

Development

Heterozygous *Dab1* Null Mutation Disrupts Neocortical and Hippocampal Development

Takao Honda,^{1,2} Yuki Hirota,¹ and  Kazunori Nakajima¹<https://doi.org/10.1523/ENEURO.0433-22.2023>

¹Department of Anatomy, Keio University School of Medicine, Tokyo 160-8582, Japan and ²Laboratory of Molecular Biology, Department of Biofunctional Analysis, Gifu Pharmaceutical University, Gifu 501-1196, Japan

Abstract

Loss-of-function mutations in Reelin and DAB1 signaling pathways disrupt proper neuronal positioning in the cerebral neocortex and hippocampus, but the underlying molecular mechanisms remain elusive. Here, we report that heterozygous *yotari* mice harboring a single autosomal recessive *yotari* mutation of *Dab1* exhibited a thinner neocortical layer 1 than wild-type mice on postnatal day (P)7. However, a birth-dating study suggested that this reduction was not caused by failure of neuronal migration. *In utero* electroporation-mediated sparse labeling revealed that the superficial layer neurons of heterozygous *yotari* mice tended to elongate their apical dendrites within layer 2 than within layer 1. In addition, the CA1 pyramidal cell layer in the caudo-dorsal hippocampus was abnormally split in heterozygous *yotari* mice, and a birth-dating study revealed that this splitting was caused mainly by migration failure of late-born pyramidal neurons. Adeno-associated virus (AAV)-mediated sparse labeling further showed that many pyramidal cells within the split cell had misoriented apical dendrites. These results suggest that regulation of neuronal migration and positioning by Reelin-DAB1 signaling pathways has unique dependencies on *Dab1* gene dosage in different brain regions.

Key words: apical dendrite; *Dab1*; haploinsufficiency; *reeler*; Reelin; *yotari*

Significance Statement

DAB1 is a cytoplasmic adaptor protein essential for transmission of the extracellular Reelin signal to cytoplasmic proteins that regulate cortical development. In this study, we found that *Dab1* is haploinsufficient for the regulation of neuronal migration but haploinsufficient for control of layer 1 thickness in the cerebral neocortex. Alternatively, the migration of a subpopulation of hippocampal pyramidal neurons is sensitive to *Dab1* gene haploinsufficiency. This study suggests that neural development in the cerebral neocortex and hippocampus are differentially sensitive to *Dab1* gene dose.

Introduction

In the mammalian cerebral neocortex, excitatory neurons are born mainly in the ventricular and subventricular zones and migrate radially toward the pial surface by passing through preexisting neuronal layers. Therefore, excitatory cortical neurons are aligned in an “early-born deep” and “late-born superficial” sequence (Cooper, 2008; Honda et al., 2011; Ohtaka-Maruyama and Okado, 2015). Radially migrating neurons express receptors for Reelin, a large secreted glycoprotein mainly produced by

Cajal-Retzius cells in the marginal zone that is critical for the positioning of excitatory neurons (D’Arcangelo et al., 1995; Hirotsune et al., 1995; Ogawa et al., 1995). Activation of the Reelin receptors apolipoprotein E receptor 2 (APOER2) and/or very low-density lipoprotein receptor (VLDLR) stimulates Src-mediated tyrosine phosphorylation of the nucleocytoplasmic-shuttling adaptor protein DAB1 (Howell et al., 1997, 2000; Trommsdorff et al., 1999; Honda and Nakajima, 2006, 2016), which in turn interacts with a host of molecular pathways controlling neuronal

Received October 23, 2022; accepted March 14, 2023; First published March 20, 2023.

The authors declare no competing financial interests.

Author contributions: T.H. and K.N. designed research; T.H. and Y.H. performed research; T.H. and K.N. analyzed data; T.H. and K.N. wrote the paper.

migration (Assadi et al., 2003; Bock et al., 2003; Pramatarova et al., 2003; Ballif et al., 2004; Chen et al., 2004; Huang et al., 2004; Feng et al., 2007; Franco et al., 2011; Jossin and Cooper, 2011; Sekine et al., 2012; Matsunaga et al., 2017). Thus, the null mutation of *Reelin* (Falconer, 1951; Montgomery et al., 1994; Bar et al., 1995; D'Arcangelo et al., 1995), the double null mutation of *Apoer2* and *Vldlr* (D'Arcangelo et al., 1999; Hiesberger et al., 1999; Trommsdorff et al., 1999), and *Dab1* null mutation (Howell et al., 1997; Sheldon et al., 1997; Yoneshima et al., 1997; Kojima et al., 2000) result in developmental defects in the cerebral neocortex, hippocampus, and cerebellum. In cerebral neocortex, for instance, *Reelin*, or *Dab1* null mutation results in the absence of layer 1 and severe neuronal migration failure (Hamburgh, 1963; Caviness, 1982; D'Arcangelo, 2005). Similarly, excessive cytosolic DAB1 protein causes severe migration failure in wild-type mice (Honda and Nakajima, 2016), suggesting that the regulation of cytosolic DAB1 protein amount is important for the migration of excitatory neurons. Naturally occurring deletions, duplications, and loss-of-function mutations of genes sometimes cause gene dosage effects on function (Veitia and Potier, 2015). For diploid organisms, the protein product from one allele is often sufficient to allow normal growth, development, and physiological function; however, a small number of genes exhibit dosage sensitivity, leading to deficits in the heterozygous state (termed haploinsufficiency). In general, genes encoding enzymes tend to be dose-insensitive, whereas genes that encode proteins with structural, transcriptional, or regulatory functions are more likely to be dose-sensitive (Kondrashov and Koonin, 2004; Morrill and Amon, 2019). DAB1 is a versatile protein that mediates multiple functions, but the underlying signaling pathways for many of these functions have not been fully elucidated. Therefore, it is important to dissect DAB1 pathways and determine the gene-dose sensitivity of each. Further, among the previous studies related to the Reelin-DAB1 signaling pathway, there are several reports showing that attenuation of Reelin signaling pathway caused defects in the cerebral cortical development

This work was supported by JSPS KAKENHI Grant Numbers JP21K06413, JP18K06508, JP24700357, JP16H06482, JP20H05688, JP22K19365, and JP20K06670; Asahi Glass Foundation; Takeda Science Foundation; Keio Gijuku Fukuzawa Memorial Fund for the Advancement of Education and Research; Keio Gijuku Academic Development Funds; Gifu Pharmaceutical University Research Fund; and Toukai Foundation for Technology.

Acknowledgments: We thank Dr. Jun-ichi Miyazaki (Osaka University, Osaka, Japan) for providing the pCAGGS, Dr. Q. Lu (Beckman Research Institute of the City of Hope) for the Dcx4kb-EGFP, Dr. S. Miyagawa (Osaka University) for the pCXN-Cre, Karel Svoboda (Howard Hughes Medical Institute) for AAV-CAG-GFP, University of Pennsylvania Penn Vector Core for pAdΔF6 and pAAV2/9, technicians of Nakajima laboratory, especially Yuki Nomura for her help in analyzing data, and all the members of the Nakajima laboratory for their helpful discussion and valuable comments.

Correspondence should be addressed to Takao Honda at takaohonda@gmail.com or Kazunori Nakajima at kazunori@keio.jp.

<https://doi.org/10.1523/ENEURO.0433-22.2023>

Copyright © 2023 Honda et al.

This is an open-access article distributed under the terms of the Creative Commons Attribution 4.0 International license, which permits unrestricted use, distribution and reproduction in any medium provided that the original work is properly attributed.

(Herrick and Cooper, 2002; Hack et al., 2007; Kohno et al., 2015; de Frutos et al., 2016; Hirota et al., 2018; Hirota and Nakajima, 2020) and might be associated with the pathogenesis of a number of neuropsychiatric disorders including schizophrenia (Impagnatiello et al., 1998; Guidotti et al., 2000), bipolar disorder (Guidotti et al., 2000), autism spectrum disorder (Fatemi et al., 2001, 2005), and Alzheimer's disease (Chin et al., 2007). However, it is not clear whether there is *Dab1* gene-dosage dependency for each reported phenotype.

To examine whether *Dab1* exhibits haploinsufficiency or haplosufficiency in various neurodevelopmental functions, we compared neocortical and hippocampal structures between wild-type and heterozygous *yotari* mice harboring a single *Dab1* null mutation (Sheldon et al., 1997; Yoneshima et al., 1997; Kojima et al., 2000). We found that heterozygous *yotari* mice at postnatal day (P)7 exhibited reduced neocortical layer 1 thickness. In addition, some neurons located in the superficial layer tended to elongate their dendrites ectopically within layer 2. Also, we found that the late-born CA1 pyramidal cell layer in the caudal hippocampus is abnormally split in heterozygous *yotari* mice. These findings suggest that the *Dab1* gene dosage is important for maintenance of the layer 1 thickness and dendrite guidance of superficial-layer neurons in the cerebral neocortex and for the migration of late-born pyramidal neurons in the caudal hippocampus.

Materials and Methods

Mice

Heterozygous *yotari* or wild-type females were mated with heterozygous *yotari* males (RRID:IMSR_RBRC05456). Noon on the day the vaginal plug was found was designated as embryonic day (E)0.5. All animal procedures were performed in accordance with the Keio University Animal Care and Use Committee's regulations, Japanese Government Law Concerning the Protection and Control of Animals, and Japanese Government Notification of Feeding and Safekeeping of Animals.

Plasmids

A fluorescent protein expression vector, pCAGGS-RG, capable of Cre-dependent switching from DsRed to enhanced green fluorescent protein (EGFP) expression, and a Cre expression vector, pDCX-Cre, expressing Cre under control of the *Doublecortin* (DCX) promoter were used for sparse labeling of neurons as has been shown before (Kohno et al., 2015). To construct an adeno-associated virus (AAV)-DCX-Cre vector, the DCX promoter was obtained from Dcx4kb-EGFP (X. Wang et al., 2007; kindly provided by Q. Lu, Beckman Research Institute of the City of Hope), Cre cDNA was obtained from pCXN-Cre (Koresawa et al., 2000; kindly provided by S. Miyagawa, Osaka University), and the AAV plasmid backbone were obtained from AAV-CAG-GFP (a kind gift from K. Svoboda, Addgene plasmid #28014; <http://n2t.net/addgene:28014>; RRID:Addgene_28014). To construct AAV-CAG-Double-floxed Inverse Orientation (DIO)-EGFP and AAV-CAG-DIO-mCherry vectors, the DIO cassette sequence information

was obtained from the double-floxed inverse ChR2-EYFP vector (Sohal et al., 2009), and the sequence was synthesized by Genscript. This DIO cassette was then inserted into the AAV-CAG backbone obtained from AAV-CAG-GFP, yielding AAV-CAG-DIO1. The cDNAs encoding EGFP and mCherry were amplified by PCR from pEGFP-N1 (Clontech) and pmCherry (Clontech), respectively, and inserted into AAV-CAG-DIO1 in reverse orientation with respect to the CAG promoter to allow Cre-dependent expression of the reporter genes. The adenovirus helper plasmid pAd Δ F6 and vector pAAV2/9 were kindly provided by the University of Pennsylvania Penn Vector Core.

Bromodeoxyuridine (BrdU) labeling

Bromodeoxyuridine (Merck) was first dissolved in sterile phosphate-buffered saline (PBS) at 10 mg/ml, and the solution was administered to pregnant dams by intraperitoneal injection at 50 μ g BrdU/g body weight on gestation days 12.5, 14.5, and 16.5.

Immunohistochemistry

Mouse pups treated as indicated were anesthetized using isoflurane and brains fixed by transcardial perfusion with 4% paraformaldehyde (PFA). Brains were then isolated, postfixed in PFA at 4°C for 2 h, washed with PBS, incubated sequentially in 10%, 20%, and 30% sucrose/PBS for cryopreservation, embedded in a mixture of optimal cutting temperature (OCT) compound (Sakura Finetek) and 30% sucrose/PBS solution, and cryosectioned in the coronal plane at 20 μ m thick. For layer marker staining, sections were washed three times (5 min/wash) in PBS containing 0.1% Tween 20 (PBStw) at room temperature (RT), autoclaved at 105°C for 5 min in 0.01 M citrate buffer (pH 6.0) for antigen retrieval, then incubated sequentially with 5% bovine serum albumin (BSA)/PBStw at RT for 5 min and primary antibodies against BRN2 (Santa Cruz Biotechnology, sc-6029; RRID:AB_2167385), RORB (Perseus Proteomics, PP-N7927-00; RRID:AB_1964364), or TBR1 (abcam, ab31940; RRID:AB_2200219) in 5% BSA/PBStw at RT for 1 h. For visualization of immunolabeling, sections were washed three times in PBStw and incubated first with Alexa 488-labeled secondary antibody against mouse IgG (Thermo Fisher Scientific, A-21202; RRID:AB_141607) or rabbit mouse IgG (Thermo Fisher Scientific, A-11008; RRID:AB_143165) with 4',6-diamidino-2-phenylindole (DAPI; Life Technologies) at RT for 1 h. After three washes in PBS, sections were mounted with PermaFluor Aqueous Mounting Medium (Thermo Fisher Scientific). For double staining with BrdU and either BRN2 or CTIP2 (official symbol is BCL11B) antibodies, sections were autoclaved, blocked with 5% BSA/PBStw, incubated with goat anti-BRN2 (Santa Cruz, sc-6029; RRID:AB_2167385) or rat anti-CTIP2 (abcam, ab18465; RRID:AB_2064130) in 5% BSA/PBStw, washed, and incubated with Alexa 555-labeled anti-goat IgG (Thermo Fisher Scientific, A-21432; RRID:AB_2535853) or Alexa 594-labeled anti-rat IgG (Thermo Fisher Scientific, A-21209; RRID:AB_2535795). Sections were rinsed with PBStw, fixed

in 4% PFA for 10 min, washed three times in PBStw (5 min/wash) to remove trace PFA, incubated with 2N HCl at 37°C for 30 min, rewashed three times in PBStw (5 min/wash) to remove HCl, blocked in 5% BSA/PBStw for 5 min, incubated with mouse anti-BrdU (BD Biosciences, 347580; RRID:AB_10015219) for 1 h, washed again three times in PBStw, and incubated with an Alexa 488-labeled secondary antibody against mouse IgG (Thermo Fisher Scientific, A-21202; RRID:AB_141607) containing DAPI for 1 h. After three washes in PBStw, sections were embedded in PermaFluor. For DAPI staining alone, cryosections were washed in PBStw for 5 min, incubated with PBStw containing DAPI for 5 min, washed with PBStw, and embedded in PermaFluor. For immunohistochemical staining of mCherry in the hippocampus, OCT-embedded brains were sectioned in the coronal plane at 100 μ m thick and floated on PBS in a 12-well plates. Selected sections were transferred to 24-well plates containing PBS, and treated with PBS containing 5% BSA and 0.5% Triton X-100 (blocking/permeabilization buffer) for 30 min to 1 h at RT on a shaker. After removal of the blocking/permeabilization buffer, sections were treated with primary antibody against RFP (Rockland, 600-401-379; RRID:AB_2209751) at 4°C overnight on a shaker, washed three times with blocking/permeabilization buffer, and incubated with Alexa Fluor 555-labeled secondary antibody against rabbit IgG (Thermo Fisher Scientific, A-31572; RRID:AB_162543) containing DAPI for 2–3 h on a shaker. After three additional washes in PBS, the sections were embedded in PermaFluor. Confocal images were acquired using an Olympus FV1000 confocal microscope (Olympus), Leica SP8 confocal microscope (Leica microsystems), or Zeiss LSM700 confocal microscope (Zeiss).

Nissl staining

For Nissl staining, OCT-embedded brains obtained from P0 or P7 pups were sectioned in the coronal plane at 20 μ m thick, and the sections floated on a small droplet of distilled water (DW) placed on a glass slide. The excess DW under the section was removed with a pipette and allowed to air dry. Then, sections were washed three times with PBS (5 min/wash), dehydrated in an ascending ethanol gradient (70%, 80%, 90%, 95%, 99%, and 100%, each for 1 min), and then rehydrated in a descending ethanol gradient (100%, 99%, 95%, 90%, 80%, and 70%, each for 1 min). Sections were treated with 0.1% cresyl violet solution for 30 min, washed with DW for 5 min, destained with 0.005% acetic acid containing absolute ethanol for 30 s, and washed with DW for 5 min. Stained sections were dehydrated in the same ascending ethanol gradient, cleared with 100% xylene, and mounted with Entellan mounting medium (Merck).

In utero electroporation

In utero electroporation was conducted as previously described (Tabata and Nakajima, 2001, 2008). We first prepared an anesthetic mixture of three drugs in PBS, 75 ng/ml medetomidine hydrochloride (Domitor; Nippon Zenyaku Kogyo), 400 ng/ml midazolam (Sandoz), and

0.5 mg/ml butorphanol (Vetorphale; Meiji Seika Pharma). Pregnant mice at E16.5 were deeply anesthetized by the three-drug mixture at 10 μl /body weight (g), and the uterus was exteriorized. Plasmid DNA solution containing 2.5 $\mu\text{g}/\mu\text{l}$ pCAGGS-RG and 200 ng/ μl pDCX-Cre supplemented with 0.1% fast green at 1:10 v/v was injected into the lateral ventricle of embryos using a glass capillary. Then, while holding the head of individual embryos with a tweezer-type electrode (CUY21; NEPA Gene) from outside the uterine wall, 35-V electric pulses were applied four times, each for 50 ms at 950-ms intervals, using an electroporator (NEPA21; NEPA Gene). The uterus was then pushed back into the abdominal cavity, and 75 ng/ml atipamezole hydrochloride (Antisedan; Nippon Zenyaku kogyo) solution dissolved in PBS was injected at the same volume as the three-drug anesthetic mixture. Electroporated mice allowed to continue gestation and fixed by transcardial perfusion with 4% PFA at P7. Cryosections were prepared as described above.

Recombinant adeno-associated virus (rAAV) preparation

Recombinant adeno-associated viruses were prepared as described previously (Burger and Nash, 2016). A mixture of plasmid DNAs including (1) AAV-DCX-Cre, pAd Δ F6, and pAAV2/9, (2) AAV-CAG-DIO-EGFP, pAd Δ F6, and pAAV2/9, or (3) AAV-CAG-DIO-mCherry, pAd Δ F6, and pAAV2/9, was used to transfect AAVpro 293T cells (Takara Bio) seeded on twenty 15-cm dishes using polyethyleneimine “Max” (PEI-Max; Polysciences). After 2 d, cells were collected and lysed by three freeze-thaw treatments and lysates treated with Benzonase nuclease (Millipore). The rAAVs were purified from the lysates by ultracentrifugation using a discontinuous gradient of iodixanol (OptiPrep; Abbott Diagnostics Technologies AS). Banded rAAVs were collected from the 40% iodixanol layer, and the iodixanol buffer exchanged to PBS and concentration of the rAAV was performed using a Vivaspin 20 ultrafiltration unit (100 kDa molecular weight cut off; Sartorius). For determination of the genomic titer, rAAVs were treated sequentially with DNaseI and Proteinase K, and the quantity of viral DNAs was determined by quantitative PCR using a StepOnePlus real-time PCR system (Applied Biosystems).

rAAV injection

New-born pups (P0) were anesthetized on ice, and injected with AAV-DCX-Cre at $\sim 6 \times 10^8$ vector genomes (vg)/ μl , AAV-CAG-DIO-EGFP at $\sim 2 \times 10^8$ vg/ μl , and AAV-CAG-DIO-mCherry at $\sim 2 \times 10^8$ vg/ μl supplemented with 1:10 (v/v) 0.1% fast green into the lateral ventricles at 3 μl per ventricle using glass capillary connected to a microinjector. The rAAV-injected pups were placed on a warming plate until they regained normal color and full typical newborn activity, and then returned to their mothers. On P7, rAAV-injected mice were fixed by transcardial perfusion of 4% PFA and 100- μm -thick brain cryosections were prepared in the coronal plane as described above.

Measurement of layer 1, cortical wall, and relative layer 1 thickness

Layer thicknesses were measured on digital images of brain coronal sections taken from the dorsolateral region of the rostral (somatosensory and auditory), middle (visual, parietal, and auditory), and caudal (visual and auditory) cortex using Fiji software (RRID:SCR_002285; Schindelin et al., 2012). To measure neocortical layer 1 thickness, a straight line was drawn along the shortest radial distance from the pial surface to the ventricular surface (Fig. 2A,H; Extended Data Fig. 2-1). Intersecting points with the pial surface, layer 1–layer 2 border, and ventricular surface were designated A, B, and C, respectively. First, layer 1 thickness between points A and B, and cortical wall thickness between points A and C were measured. Then, a point A + 1 located 100 μm to the right of point A was drawn on the pial surface. Similarly, points A + 2 to A + 5 were drawn on the pial surface to the right of A + 1, while points A – 1 to A – 5 were drawn on the pial surface to the left of point A. Straight lines were drawn toward the ventricular surface from points A + 1 to A + 5 and A – 1 to A – 5. These lines were measured as layer 1 thickness and cortical wall thickness, respectively, using Fiji software. Measurements were performed using six P7 brains from six different litters. Relative layer 1 thickness was calculated by dividing layer 1 thickness by cortical wall thickness and multiplying by 100. Measurement results were compared between groups by independent samples Student's *t* test using the R language environment (R Foundation for Statistical Computing; <https://www.r-project.org/>; RRID:SCR_001905) as described in Table 1.

Measurements of relative cell position and distance from the ventricular surface

Distances from the ventricular surface to marker-positive cells (D1; see Fig. 3B), distances from the ventricular surface to the pial surface through each of these cells (D2; see Fig. 3B), and distances from the ventricular surface to BrdU/BRN2 double-positive cells (Fig. 4) were measured using Fiji software. Relative position was then calculated as $D1/D2 \times 10$. These measurements were performed on three brains obtained from three different litters, and results were compared between groups by independent samples Student's *t* test, unpaired Welch's *t* test, or Mann–Whitney *U* test using the R language environment as described in Table 1.

Measurement of neocortical layer thickness by the distribution of layer marker-positive cells

For quantitative comparisons, we defined layer thickness as the distance between the 20th and 80th percentile of layer marker-positive cells (Extended Data Fig. 3-2A). The markers used were TBR1, RORB, or BRN2. Measurement was performed using coronal sections of somatosensory, parietal, and visual cortices obtained from three brains from different litters. Then the average thickness of each brain along the rostro-caudal axis was calculated. Results were compared

Table 1: Summary of statistical analyses

Figure number	Panel	Comparison	Data structure: normality	Data structure: homoscedasticity	Type of test	95% confidence interval/Z	p-value
Fig. 2	I	Rostral: wild type vs heterozygote	Normal distribution Shapiro–Wilk normality test wild type: $W = 0.92806$, p -value = 0.5652 heterozygote: $W = 0.79679$, p -value = 0.05498	Equal variance F test p -value = 0.3117	Unpaired Student's t test	12.43746 to 40.41903	0.002
Fig. 2	I	Middle: wild type vs heterozygote	Normal distribution Shapiro–Wilk normality test wild type: $W = 0.92585$, p -value = 0.5484 heterozygote: $W = 0.94264$, p -value = 0.6805	Equal variance F test p -value = 0.4658	Unpaired Student's t test	10.76698 to 42.59023	0.004
Fig. 2	I	Caudal: wild type vs heterozygote	Normal distribution Shapiro–Wilk normality test wild type: $W = 0.956$, p -value = 0.7885 heterozygote: $W = 0.90402$, p -value = 0.3982	Equal variance F test p -value = 0.6094	Unpaired Student's t test	13.47947 to 41.17302	0.001
Fig. 2	J	Rostral: wild type vs heterozygote	Normal distribution Shapiro–Wilk normality test wild type: $W = 0.93972$, p -value = 0.657 heterozygote: $W = 0.92768$, p -value = 0.5623	Equal variance F test p -value = 0.178	Unpaired Student's t test	1.766226 to 5.743795	0.002
Fig. 2	J	Middle: wild type vs heterozygote	Normal distribution Shapiro–Wilk normality test wild type: $W = 0.97022$, p -value = 0.8939 heterozygote: $W = 0.98581$, p -value = 0.9765	Equal variance F test p -value = 0.3674	Unpaired Student's t test	1.605875 to 5.699706	0.003
Fig. 2	J	Caudal: wild type vs heterozygote	Normal distribution Shapiro–Wilk normality test wild type: $W = 0.97971$, p -value = 0.9501 heterozygote: $W = 0.85301$, p -value = 0.1664	Equal variance F test p -value = 0.658	Unpaired Student's t test	2.105032 to 6.101853	0.001
Fig. 2	K	Rostral: wild type vs heterozygote	Normal distribution Shapiro–Wilk normality test wild type: $W = 0.96263$, p -value = 0.8398 heterozygote: $W = 0.95556$, p -value = 0.7849	Equal variance F test p -value = 0.3327	Unpaired Student's t test	–203.52664 to 24.79879	0.112
Fig. 2	K	Middle: wild type vs heterozygote	Normal distribution Shapiro–Wilk normality test wild type: $W = 0.90479$, p -value = 0.403 heterozygote: $W = 0.91236$, p -value = 0.4521	Equal variance F test p -value = 0.9113	Unpaired Student's t test	–120.71312 to 31.80191	0.223
Fig. 2	K	Caudal: wild type vs heterozygote	Normal distribution Shapiro–Wilk normality test wild type: $W = 0.8622$, p -value = 0.1969 heterozygote: $W = 0.89865$, p -value = 0.366	Equal variance F test p -value = 0.2966	Unpaired Student's t test	–114.245014 to 4.374468	0.066
Fig. 3	C	TBR1 (rostral): wild type vs heterozygote	Normal distribution Shapiro–Wilk normality test wild type: $W = 0.87838$, p -value = 0.3197 heterozygote: $W = 0.99953$, p -value = 0.9585	Unequal variance F test p -value = 0.03097	Unpaired Welch's t test	–0.7341526 to 0.7142779	0.959
Fig. 3	C	TBR1 (middle): wild type vs heterozygote	Normal distribution Shapiro–Wilk normality test wild type: $W = 0.95681$, p -value = 0.6002 heterozygote: $W = 0.89516$, p -value = 0.3703	Equal variance F test p -value = 0.8262	Unpaired Student's t test	–0.7341526 to 0.7142779	0.543
Fig. 3	C	TBR1 (caudal): wild type vs heterozygote	Normal distribution Shapiro–Wilk normality test wild type: $W = 0.92614$, p -value = 0.4743 heterozygote: $W = 0.85654$, p -value = 0.2581	Equal variance F test p -value = 0.7396	Unpaired Student's t test	–0.7341526 to 0.7142779	0.061
Fig. 3	C	RORb (rostral): wild type vs heterozygote	Normal distribution Shapiro–Wilk normality test wild type: $W = 0.83679$, p -value = 0.2057 heterozygote: $W = 0.91815$, p -value = 0.4458	Equal variance F test p -value = 0.1755	Unpaired Student's t test	–0.7304762 to 0.8176759	0.845
Fig. 3	C	RORb (middle): wild type vs heterozygote	Normal distribution Shapiro–Wilk normality test wild type: $W = 0.81895$, p -value = 0.1606 heterozygote: $W = 0.92359$, p -value = 0.4651	Equal variance F test p -value = 0.666	Unpaired Student's t test	–0.7304762 to 0.8176759	0.870
Fig. 3	C	RORB (caudal): wild type vs heterozygote	Normal distribution Shapiro–Wilk normality test wild type: $W = 0.85562$, p -value = 0.2556 heterozygote: $W = 0.98158$, p -value = 0.74	Equal variance F test p -value = 0.07155	Unpaired Student's t test	–2.202504 to 1.445244	0.486

(Continued)

Table 1: Continued

Figure number	Panel	Comparison	Data structure: normality	Data structure: homoscedasticity	Type of test	95% confidence interval/Z	p-value
Fig. 3	C	BRN2 (rostral): wild type vs heterozygote	Normal distribution Shapiro–Wilk normality test wild type: $W = 0.99286$, p -value = 0.8385 heterozygote: $W = 0.98261$, p -value = 0.7474	Equal variance F test p -value = 0.7735	Unpaired Student's t test	–1.8201310 to 0.7466688	0.305
Fig. 3	C	BRN2: (middle) wild type vs heterozygote	Non-normal distribution Shapiro–Wilk normality test wild type: $W = 0.99043$, p -value = 0.8129 heterozygote: $W = 0.76126$, p -value = 0.02503	Equal variance F test p -value = 0.4921	Mann–Whitney U test	$Z = 0.65465$	0.700
Fig. 3	C	BRN2 (caudal): wild type vs heterozygote	Normal distribution Shapiro–Wilk normality test wild type: $W = 0.984$, p -value = 0.7578 heterozygote: $W = 0.93876$, p -value = 0.5224	Equal variance F test p -value = 0.3267	Unpaired Student's t test	–2.011466 to 1.115294	0.413
Fig. 3	D	TBR1 (rostral): wild type vs heterozygote	Normal distribution Shapiro–Wilk normality test wild type: $W = 0.99311$, p -value = 0.8413 heterozygote: $W = 0.8151$, p -value = 0.1511	Equal variance F test p -value = 0.5543	Unpaired Welch's t test	–42.65128 to 80.04344	0.445
Fig. 3	D	TBR1 (middle): wild type vs heterozygote	Normal distribution Shapiro–Wilk normality test wild type: $W = 0.81232$, p -value = 0.1443 heterozygote: $W = 0.99621$, p -value = 0.8824	Equal variance F test p -value = 0.9107	Unpaired Student's t test	–2.011466 to 1.115294	0.215
Fig. 3	D	TBR1 (caudal): wild type vs heterozygote	Normal distribution Shapiro–Wilk normality test wild type: $W = 0.99479$, p -value = 0.862 heterozygote: $W = 0.90284$, p -value = 0.3946	Equal variance F test p -value = 0.362	Unpaired Student's t test	–77.58617 to 17.77541	0.157
Fig. 3	D	RORb (rostral): wild type vs heterozygote	Normal distribution Shapiro–Wilk normality test wild type: $W = 0.92163$, p -value = 0.4581 heterozygote: $W = 0.94029$, p -value = 0.5286	Equal variance F test p -value = 0.2323	Unpaired Student's t test	–101.65007 to 82.43556	0.786
Fig. 3	D	RORb (middle): wild type vs heterozygote	Normal distribution Shapiro–Wilk normality test wild type: $W = 0.8246$, p -value = 0.1747 heterozygote: $W = 0.95008$, p -value = 0.5697	Equal variance F test p -value = 0.8781	Unpaired Student's t test	–95.84147 to 113.25092	0.829
Fig. 3	D	RORb (caudal): wild type vs heterozygote	Normal distribution Shapiro–Wilk normality test wild type: $W = 0.96848$, p -value = 0.6591 heterozygote: $W = 0.96668$, p -value = 0.6494	Equal variance F test p -value = 0.9331	Unpaired Student's t test	–146.25097 to 33.68333	0.157
Fig. 3	D	BRN2 (rostral): wild type vs heterozygote	Normal distribution Shapiro–Wilk normality test wild type: $W = 0.85$, p -value = 0.2404 heterozygote: $W = 0.88077$, p -value = 0.3267	Equal variance F test p -value = 0.9132	Unpaired Student's t test	–259.03986 to 83.37571	0.228
Fig. 3	D	BRN2: (middle) wild type vs heterozygote	Normal distribution Shapiro–Wilk normality test wild type: $W = 0.90474$, p -value = 0.4008 heterozygote: $W = 0.9984$, p -value = 0.9235	Equal variance F test p -value = 0.6548	Unpaired Student's t test	–211.6771 to 138.7905	0.595
Fig. 3	D	BRN2 (caudal): wild type vs heterozygote	Normal distribution Shapiro–Wilk normality test wild type: $W = 0.98321$, p -value = 0.7518 heterozygote: $W = 0.95459$, p -value = 0.5899	Equal variance F test p -value = 0.7567	Unpaired Student's t test	–259.03986 to 83.37571	0.228
Fig. 4	B	Rostral: wild type vs heterozygote	Normal distribution Shapiro–Wilk normality test wild type: $W = 0.88946$, p -value = 0.3527 heterozygote: $W = 0.90024$, p -value = 0.3863	Equal variance F test p -value = 0.3471	Unpaired Student's t test	–0.5520192 to 0.2715238	0.398
Fig. 4	B	Middle: wild type vs heterozygote	Normal distribution Shapiro–Wilk normality test wild type: $W = 0.97423$, p -value = 0.6921 heterozygote: $W = 0.77489$, p -value = 0.05587	Equal variance F test p -value = 0.8878	Unpaired Student's t test	–0.9814349 to 0.2605900	0.182

(Continued)

Table 1: Continued

Figure number	Panel	Comparison	Data structure: normality	Data structure: homoscedasticity	Type of test	95% confidence interval/Z	p-value
Fig. 4	B	Caudal: wild type vs heterozygote	Normal distribution Shapiro–Wilk normality test wild type: $W = 0.96518$, p -value = 0.6415 heterozygote: $W = 0.94166$, p -value = 0.5341	Equal variance F test p -value = 0.1779	Unpaired Student's t test	–1.381734 to 0.107321	0.076
Fig. 4	C	Rostral: wild type vs heterozygote	Normal distribution Shapiro–Wilk normality test wild type: $W = 0.98083$, p -value = 0.7347 heterozygote: $W = 0.99765$, p -value = 0.9075	Equal variance F test p -value = 0.9134	Unpaired Student's t test	–334.0189 to 298.0080	0.882
Fig. 4	C	Middle: wild type vs heterozygote	Normal distribution Shapiro–Wilk normality test wild type: $W = 0.83705$, p -value = 0.2064 heterozygote: $W = 0.95242$, p -value = 0.5801	Equal variance F test p -value = 0.6733	Unpaired Student's t test	–157.30316 to 97.03834	0.547
Fig. 4	C	Caudal: wild type vs heterozygote	Normal distribution Shapiro–Wilk normality test wild type: $W = 0.97936$, p -value = 0.7246 heterozygote: $W = 0.99965$, p -value = 0.9645	Equal variance F test p -value = 0.9995	Unpaired Student's t test	–61.38874 to 29.16489	0.379
Fig. 5	B	E12.5 BrdU -> P9 fix wild type vs heterozygote	Normal distribution Shapiro–Wilk normality test wild type: $W = 0.84955$, p -value = 0.2247 heterozygote: $W = 0.90757$, p -value = 0.4696	Equal variance F test p -value = 0.06273	Unpaired Student's t test	–12.9173912 to 0.5582761	0.066
Fig. 5	B	E14.5 BrdU -> P9 fix wild type vs heterozygote	Non-normal distribution Shapiro–Wilk normality test wild type: $W = 0.78785$, p -value = 0.08216 heterozygote: $W = 0.89427$, p -value = 0.4031	Unequal variance F test p -value = 0.03346	Unpaired Welch's t test	–46.46305 to –18.39430	0.004
Fig. 5	B	E16.5 BrdU -> P9 fix wild type vs heterozygote	Normal distribution Shapiro–Wilk normality test wild type: $W = 0.81206$, p -value = 0.1257 heterozygote: $W = 0.96273$, p -value = 0.7961	Equal variance F test p -value = 0.6301	Unpaired Student's t test	–45.14384 to –13.72628	0.004
Fig. 5	D	E16.5 BrdU -> P3 fix wild type vs heterozygote	Normal distribution Shapiro–Wilk normality test wild type: $W = 0.87183$, p -value = 0.3007 heterozygote: $W = 0.79291$, p -value = 0.09768	Equal variance F test p -value = 0.7788	Unpaired Student's t test	–25.481745 to –5.383604	0.013
Fig. 6	F	Wild type vs heterozygote (normal position)	Normal distribution Shapiro–Wilk normality test wild type: $W = 0.99526$, p -value = 0.8685 heterozygote (normal position): $W = 0.90932$, p -value = 0.4158	Equal variance Bartlett test p -value = 0.0678	Tukey–Kramer test	–437.8421 to 150.364845	0.398
Fig. 6	F	Wild type vs heterozygote (ectopic position)	Normal distribution Shapiro–Wilk normality test wild type: $W = 0.99526$, p -value = 0.8685 heterozygote (ectopic position): $W = 0.82469$, p -value = 0.09685	Equal variance Bartlett test p -value = 0.0678	Tukey–Kramer test	–514.7175 to –5.315335	0.046
Fig. 6	F	Heterozygote (normal position) vs heterozygote (ectopic position)	Normal distribution Shapiro–Wilk normality test heterozygote (normal position): $W = 0.90932$, p -value = 0.4158 heterozygote (ectopic position): $W = 0.82469$, p -value = 0.09685	Equal variance Bartlett test p -value = 0.0678	Tukey–Kramer test	–138.4233 to 370.978869	0.443
Fig. 6	G	Wild type vs heterozygote (normal position)	Normal distribution Shapiro–Wilk normality test wild type: $W = 0.8105$, p -value = 0.1398 heterozygote (normal position): $W = 0.9134$, p -value = 0.4295	Equal variance Bartlett test p -value = 0.3671	Tukey–Kramer test	–6.306416 to 2.5699079	0.496
Fig. 6	G	Wild type vs heterozygote (ectopic position)	Normal distribution Shapiro–Wilk normality test wild type: $W = 0.8105$, p -value = 0.1398 heterozygote (ectopic position): $W = 0.91542$, p -value = 0.473	Equal variance Bartlett test p -value = 0.3671	Tukey–Kramer test	–6.826894 to 0.8602276	0.131

(Continued)

Table 1: Continued

Figure number	Panel	Comparison	Data structure: normality	Data structure: homoscedasticity	Type of test	95% confidence interval/Z	p-value
Fig. 6	G	Heterozygote (normal position) vs heterozygote (ectopic position)	Normal distribution Shapiro–Wilk normality test heterozygote (normal position): $W = 0.9134$, p -value = 0.4295 heterozygote (ectopic position): $W = 0.91542$, p -value = 0.473	Equal variance Bartlett test p -value = 0.3671	Tukey–Kramer test	–2.728482 to 4.9586403	0.707
Fig. 6	H	Wild type vs heterozygote (normal position)	Normal distribution Shapiro–Wilk normality test wild type: $W = 0.98032$, p -value = 0.7312 heterozygote (normal position): $W = 0.97948$, p -value = 0.7255	Unequal variance Bartlett test p -value = 0.0005376	Steel–Dwass test		1.000
Fig. 6	H	Wild type vs heterozygote (ectopic position)	Normal distribution Shapiro–Wilk normality test wild type: $W = 0.98032$, p -value = 0.7312 heterozygote (ectopic position): $W = 0.92588$, p -value = 0.5487	Unequal variance Bartlett test p -value = 0.0005376	Steel–Dwass test		0.256
Fig. 6	H	Heterozygote (normal position) vs heterozygote (ectopic position)	Normal distribution Shapiro–Wilk normality test heterozygote (normal position): $W = 0.97948$, p -value = 0.7255 heterozygote (ectopic position): $W = 0.92588$, p -value = 0.5487	Unequal variance Bartlett test p -value = 0.0005376	Steel–Dwass test		0.256
Fig. 7	E	Wild type vs heterozygote	Normal distribution Shapiro–Wilk normality test wild type: $W = 0.98136$, p -value = 0.7384 heterozygote: $W = 0.82619$, p -value = 0.1787	Equal variance F test p -value = 0.1953	Unpaired Student's t test	–27.896256 to 6.444708	0.158
Fig. 7	F	Wild type vs heterozygote	Normal distribution Shapiro–Wilk normality test wild type: $W = 0.98334$, p -value = 0.7528 heterozygote: $W = 0.79961$, p -value = 0.1136	Equal variance F test p -value = 0.5522	Unpaired Student's t test	–18.92532 to 75.37736	0.172
Fig. 7	G	L1: wild type vs heterozygote	Normal distribution Shapiro–Wilk normality test wild type: $W = 0.89302$, p -value = 0.3636 heterozygote: $W = 0.89602$, p -value = 0.3729	Equal variance F test p -value = 0.9608	Unpaired Student's t test	49.88475 to 142.24042	0.004
Fig. 7	G	L2: wild type vs heterozygote	Normal distribution Shapiro–Wilk normality test wild type: $W = 0.95785$, p -value = 0.6051 heterozygote: $W = 0.8297$, p -value = 0.1876	Equal variance F test p -value = 0.1826	Unpaired Student's t test	–113.18916 to –22.48398	0.021
Fig. 7	H	Wild type vs heterozygote	Non-normal distribution Shapiro–Wilk normality test wild type: $W = 0.76125$, p -value = 0.02501 heterozygote: $W = 0.77171$, p -value = 0.0486		Mann–Whitney U test	$Z = -0.65465$	0.700
Fig. 7	I	L1: wild type vs heterozygote	Normal distribution Shapiro–Wilk normality test wild type: $W = 0.80732$, p -value = 0.1321 heterozygote: $W = 0.998$, p -value = 0.9147	Equal variance F test p -value = 0.6222	Unpaired Student's t test	2.056330 to 4.188658	0.001
Fig. 7	I	L2: wild type vs heterozygote	Non-normal distribution Shapiro–Wilk normality test wild type: $W = 0.80371$, p -value = 0.1234 heterozygote: $W = 0.96722$, p -value = 0.6523	Equal variance F test p -value = 0.2364	Unpaired Student's t test	–6.311426 to –0.491803	0.032
Extended Data Fig. 3-1	B	Rostral: wild type vs heterozygote	Non-normal distribution Shapiro–Wilk normality test wild type: $W = 0.85766$, p -value = 0.1813 heterozygote: $W = 0.82895$, p -value = 0.1053	Equal variance F test p -value = 0.7773	Unpaired Student's t test	–0.0421572482 to 0.0007444148	0.057

(Continued)

Table 1: Continued

Figure number	Panel	Comparison	Data structure: normality	Data structure: homoscedasticity	Type of test	95% confidence interval/Z	p-value
Extended Data Fig. 3-1	B	Middle: wild type vs heterozygote	Non-normal distribution Shapiro–Wilk normality test wild type: $W = 0.88419$, p -value = 0.2889 heterozygote: $W = 0.92997$, p -value = 0.5799	Equal variance F test p -value = 0.1479	Unpaired Student's t test	–0.033846035 to –0.002103765	0.030
Extended Data Fig. 3-1	B	Caudal: wild type vs heterozygote	Non-normal distribution Shapiro–Wilk normality test wild type: $W = 0.93585$, p -value = 0.6259 heterozygote: $W = 0.90844$, p -value = 0.4262	Equal variance F test p -value = 0.9502	Unpaired Student's t test	–0.030801905 to –0.009642128	0.002
Extended Data Fig. 3-1	C	Rostral: wild type vs heterozygote	Non-normal distribution Shapiro–Wilk normality test wild type: $W = 0.90901$, p -value = 0.4299 heterozygote: $W = 0.93146$, p -value = 0.5914	Unequal variance F test p -value = 0.02958	Unpaired Welch's t test	–164.72649 to 42.39315	0.199
Extended Data Fig. 3-1	C	Middle: wild type vs heterozygote	Non-normal distribution Shapiro–Wilk normality test wild type: $W = 0.93329$, p -value = 0.6057 heterozygote: $W = 0.97804$, p -value = 0.9414	Equal variance F test p -value = 0.1447	Unpaired Student's t test	–187.04365 to –24.62301	0.016
Extended Data Fig. 3-1	C	Caudal: wild type vs heterozygote	Non-normal distribution Shapiro–Wilk normality test wild type: $W = 0.82064$, p -value = 0.08938 heterozygote: $W = 0.80381$, p -value = 0.06359	Equal variance F test p -value = 0.6413	Unpaired Student's t test	–232.61149 to 44.94482	0.163
Extended Data Fig. 3-1	D	Rostral: wild type vs heterozygote	Non-normal distribution Shapiro–Wilk normality test wild type: $W = 0.71196$, p -value = 0.008242 heterozygote: $W = 0.93999$, p -value = 0.6591		Mann–Whitney U test	$Z = -0.64051$	0.589
Extended Data Fig. 3-1	D	Middle: wild type vs heterozygote	Non-normal distribution Shapiro–Wilk normality test wild type: $W = 0.87287$, p -value = 0.2379 heterozygote: $W = 0.94396$, p -value = 0.6912	Equal variance F test p -value = 0.8054	Unpaired Student's t test	–953.6398 to 772.9249	0.820
Extended Data Fig. 3-1	D	Caudal: wild type vs heterozygote	Non-normal distribution Shapiro–Wilk normality test wild type: $W = 0.89833$, p -value = 0.3642 heterozygote: $W = 0.68099$, p -value = 0.003873		Mann–Whitney U test	$Z = -0.2445$	0.853
Extended Data Fig. 3-2		TBR1: wild type vs heterozygote	Non-normal distribution Shapiro–Wilk normality test wild type: $W = 0.93052$, p -value = 0.4906 heterozygote: $W = 0.8333$, p -value = 0.1967	Equal variance F test p -value = 0.3502	Unpaired Student's t test	–50.99473 to 10.79854	0.145
Extended Data Fig. 3-2		RORB: wild type vs heterozygote	Non-normal distribution Shapiro–Wilk normality test wild type: $W = 0.77427$, p -value = 0.05444 heterozygote: $W = 0.90745$, p -value = 0.4096	Equal variance F test p -value = 0.1612	Unpaired Student's t test	–38.81443 to –12.39362	0.006
Extended Data Fig. 3-2		Brn2: wild type vs heterozygote	Non-normal distribution Shapiro–Wilk normality test wild type: $W = 0.9922$, p -value = 0.8311 heterozygote: $W = 0.87014$, p -value = 0.2959	Equal variance F test p -value = 0.7895	Unpaired Student's t test	–57.77120 to 86.12194	0.609
Extended Data Fig. 4-1	A	Wild type vs heterozygote	Non-normal distribution Shapiro–Wilk normality test wild type: $W = 0.97442$, p -value = 0.9297 heterozygote: $W = 0.77181$, p -value = 0.009691		Mann–Whitney U test	$Z = -1.7228$	0.089

(Continued)

Table 1: Continued

Figure number	Panel	Comparison	Data structure: normality	Data structure: homoscedasticity	Type of test	95% confidence interval/Z	<i>p</i> -value
Extended Data Fig. 4-1	B	Wild type vs heterozygote	Non-normal distribution Shapiro–Wilk normality test wild type: $W = 0.96529$, p -value = 0.8517 heterozygote: $W = 0.85836$, p -value = 0.09203	Equal variance <i>F</i> test p -value = 0.7867	Unpaired Student's <i>t</i> test	–22.37795 to 178.75553	0.119
Extended Data Fig. 4-1	C	Wild type vs heterozygote	Non-normal distribution Shapiro–Wilk normality test wild type: $W = 0.93988$, p -value = 0.5806 heterozygote: $W = 0.96297$, p -value = 0.8289	Equal variance <i>F</i> test p -value = 0.3549	Unpaired Student's <i>t</i> test	–20.29773 to 17.85329	0.894
Extended Data Fig. 4-1	D	Wild type vs heterozygote	Non-normal distribution Shapiro–Wilk normality test wild type: $W = 0.90943$, p -value = 0.3119 heterozygote: $W = 0.96112$, p -value = 0.8099	Equal variance <i>F</i> test p -value = 0.6479	Unpaired Student's <i>t</i> test	–75.85538 to 144.40307	0.519
Extended Data Fig. 4-1	E	Wild type vs heterozygote	Non-normal distribution Shapiro–Wilk normality test wild type: $W = 0.88971$, p -value = 0.1982 heterozygote: $W = 0.97785$, p -value = 0.9523	Equal variance <i>F</i> test p -value = 0.944	Unpaired Student's <i>t</i> test	–47.06784 to 102.62339	0.443
Extended Data Fig. 4-1	F	Wild type vs heterozygote	Non-normal distribution Shapiro–Wilk normality test wild type: $W = 0.8859$, p -value = 0.181 heterozygote: $W = 0.86775$, p -value = 0.1163	Equal variance <i>F</i> test p -value = 0.6467	Unpaired Student's <i>t</i> test	–244.6362 to 902.2204	0.242

between groups by independent samples Student's *t* test using the R language environment.

Measurement of pyramidal neuron apical dendrite angle in cerebral neocortex and hippocampus

To measure the apical dendrite angle of pyramidal neurons in the cerebral neocortex, a perpendicular line was drawn from the pial surface to the center of the target cell body, from which another straight line was drawn to the first branch point of the apical dendrite (Fig. 7D,E). The angle between these two straight lines was measured using Fiji software and defined as the apical dendrite angle. To measure the apical dendrite angle of hippocampal pyramidal neurons, a line perpendicular to the pyramidal cell layer was drawn to the center of the target cell body and another from the target cell body center to the first branch point of the apical dendrite (Fig. 6H). The angle between the lines was then measured using Fiji software. Measurements were conducted on more than three brains, all obtained from different litters. Angles were compared between groups by the Steel–Dwass test using the R language environment as described in Table 1.

Measurement of apical dendrite length and number of branching points within neocortical layer 1 or layers 2

Sparsely labeled EGFP-positive cells using electroporation as described above were selected, and their apical dendrite length and number of apical dendrite branching points within layer 1 and layer 2 were measured using Fiji software, respectively. Brains were obtained from more than three mice, each from different litters, and results

compared between groups by independent samples Student's *t* test or Mann–Whitney *U* test using the R language environment as described in Table 1.

Measurement of the total apical dendrite length and total number of branching points in the hippocampus

Total apical dendrite length and branch point number were determined using Fiji software. Measurements were performed using more than three brains derived from different litters, and results compared between groups by Tukey–Kramer test using the R language environment as described in Table 1.

Experimental design and statistical analysis

Experimental design details, sample sizes, and results of statistical analyses are presented in the corresponding Materials and Methods and Results sections, figure legends, and Table 1. Mice of either sex were used throughout the study. Exact *p*-values are listed on Table 1 and also labeled on figures. A $p < 0.05$ was considered significant for all tests.

Results

Heterozygous *yotari* mutant mice exhibit a thinner neocortical layer 1 than wild-type mice and a split CA1 pyramidal cell layer in the caudal hippocampus

To examine whether neuronal positioning is disrupted by reduced *Dab1* gene expression, we compared the cytoarchitecture of the cerebral neocortex and hippocampus between wild-type and heterozygous *yotari* mutant mice using Nissl staining at P0 and P7. There

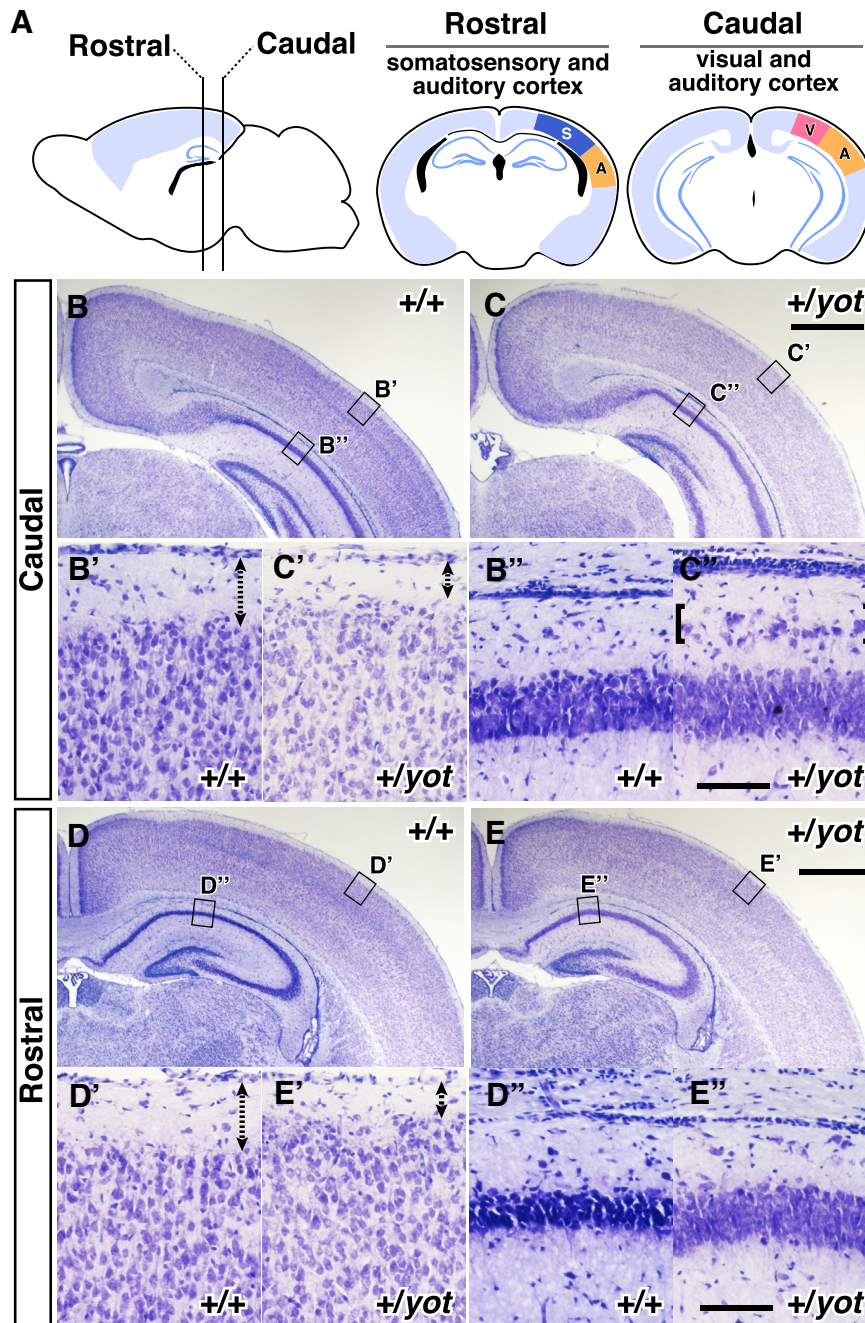


Figure 1. Cortical layer 1 is thinner and the CA1 pyramidal cell layer is split in the caudal hippocampus of heterozygous *yotari* mutant mice. **A**, Schematic illustrations of the analyzed brain regions in **B–E''**. S: somatosensory cortex; A: auditory cortex; V: visual cortex. **B–E''**, Nissl-stained coronal brain sections of the caudal region containing the visual and auditory cortices (**B–C''**, Caudal) and rostral region containing the somatosensory and auditory cortices (**D–E''**, Rostral) from wild-type mice ($+/+$; **B**, **B'**, **B''**, **D**, **D'**, **D''**) and heterozygous *yotari* mice ($+/yot$; **C**, **C'**, **C''**, **E**, **E'**, **E''**) at P7. Enlarged views from the regions enclosed by rectangles in **B**, **C**, **D**, **E** are shown in **B'**, **B''**, **C'**, **C''**, **D'**, **D''**, **E'**, **E''**, respectively. **B'** and **C'** show auditory cortex, and **D'** and **E'** show somatosensory cortex. Layer 1 is shown by dashed arrows with two ends (**B'**, **C'**, **D'**, **E'**). Ectopic cells in heterozygous *yotari* mutant mice are indicated by brackets in **C''**. Scale bars: 1 mm (**B**, **C**, **D**, **E**) and 10 μm (**B'**, **B''**, **C'**, **C''**, **D'**, **D''**, **E'**, **E''**).

were no obvious differences in cortical layer structure between genotypes at P0 (Extended Data Fig. 1-1), but layer 1 was significantly thinner in both the rostral brain region containing somatosensory and auditory cortices (Fig. 1, Rostral) and caudal brain region containing visual and auditory cortices (Fig. 1, Caudal) of

P7 heterozygous *yotari* mutant mice compared with P7 wild-type mice.

To quantitatively evaluate potential differences in neocortical layer thickness between wild-types and heterozygous *yotari* mutant mice, we stained nuclei in coronal brain sections with DAPI (Fig. 2B–G, B'–G') and measured

continued

Materials and Methods and Extended Data Figure 2-1 for details. **I–K**, Combination of dot, violin, and scatter plots showing layer 1 thickness (**I**), relative layer 1 thickness (**J**), and cortical wall thickness (**K**) across brain regions. The black dot and bar in the leftmost dot plot indicate mean and SD, respectively, and each gray dot indicates the mean from one individual brain. Each black circle in the scatter plot is a raw datapoint. Measurement was performed on six brains obtained from six different litters ($n=6$). Three different coronal sections were obtained from the caudal, middle, and rostral brain of each mouse as shown in **A**, and 11 positions were analyzed per brain region. Mean values were then calculated for each brain region. Genotype differences were analyzed by Student's t test. $**p < 0.01$, ns (not significant) $p > 0.05$. Scale bars: 200 μm (**B–G**) and 50 μm (**B'–G'**).

layer 1 thickness (Fig. 2I) and cortical wall thickness (Fig. 2K; see Materials and Methods). Consistent with Nissl staining, layer 1 thickness (Fig. 2I) of the rostral brain region containing somatosensory and auditory cortices (Fig. 2; Extended Data Fig. 2-1, Rostral), middle brain region containing visual, parietal, and auditory cortices (Fig. 2; Extended Data Fig. 2-1, Middle), and caudal brain region containing visual and auditory cortices (Fig. 2; Extended Data Fig. 2-1, Caudal) were significantly reduced in *yotari* heterozygous mice compared with wild-type mice. Moreover, relative layer 1 thickness, calculated as the ratio of layer 1 thickness to cortical wall thickness, was also reduced in rostral, middle, and caudal regions of heterozygous *yotari* mouse neocortex (Fig. 2J). In the hippocampus as well, layer structure was abnormal in heterozygous *yotari* mice, but was manifested by an abnormal split in the caudal CA1 pyramidal cell layer (Fig. 1C,C').

The RORB-positive layer 4 but not TBR1-positive and BRN2-positive layers 5/6 and 2 are expanded in the neocortex of heterozygous *yotari* mice

The reduced layer 1 thickness observed among heterozygous *yotari* mice by Nissl and DAPI staining may result from disruption of the cortical layer structure and/or positional changes in cortical neurons (as seen in *reeler* and *yotari* homozygous mutants; Howell et al., 1997; Sheldon et al., 1997; Yoneshima et al., 1997; Trommsdorff et al., 1999). To distinguish between these possibilities, we examined whether relative position or distance from the ventricular surface of cortical neurons is differed between genotypes by staining coronal brain sections with antibodies specifically targeting layer 5/6 neurons (TBR1), layer 4 neurons (RORB), or layer 2/3 neurons (BRN2), and measured individual cell positions (Fig. 3). While there were no significant differences in relative position of cells (Fig. 3C), scatter plots revealed that BRN2-positive layer 2/3 neurons tended to be located farther from the ventricular surface in heterozygous *yotari* mice than wild-type mice (Fig. 3D), suggesting that layer 2/3 is shifted by cell dispersion into layer 1.

We then examined whether this reduction in layer 1 thickness was accompanied by changes in other layers. Briefly, we defined a 200- μm wide measurement area from the layer 1–2 boundary to the ventricular surface (Extended Data Fig. 3-1A) and examined layer 2/3, 4, and 5/6 area (Extended Data Fig. 3-1B), cell number (Extended Data Fig. 3-1C), and cell density (Extended Data Fig. 3-1D) in somatosensory (Rostral), parietal (Middle), and visual (Caudal) cortices. We found that the measured area was significantly larger in the middle and caudal brain regions of heterozygous *yotari* mice

(Extended Data Fig. 3-1B). There was also a significant increase in cell number within the middle brain region of heterozygous *yotari* mice, and a numerical increase in both rostral and caudal brain regions that did not reach statistical significance (Extended Data Fig. 3-1C). In contrast, there were no differences in cell density between wild-type and heterozygous *yotari* mutant mice (Extended Data Fig. 3-1D).

We also examined the thickness of each layer by measuring the distributions of neurons immunopositive for layer-specific markers (Extended Data Fig. 3-2). For comparison, we defined the layer thickness as the length along which the 20th–80th percentile population of layer marker-positive cells is distributed (Extended Data Fig. 3-2A) as it was difficult to clearly determine the boundaries of layers based on the distribution of the all layer marker positive cells. This analysis revealed no significant difference in TBR1-positive layer 5/6 thickness or BRN2-positive layer 2/3 thickness, but RORB-positive layer 4 thickness was greater in heterozygous *yotari* mice than wild-type mice (Extended Data Fig. 3-2B). These results suggest that a half reduction in the *Dab1* gene dosage causes a decrease in layer 1 thickness as well as an increase in the area of the neocortical region from layer 2 to the ventricular surface and cell number with an expansion of RORB-positive layer 4 thickness.

To further explore whether the reduction of DAB1 protein causes superficial positional shift of the superficial layer neurons, late-born neurons were labeled by BrdU at E16.5 and visualized at P9 (Fig. 4A) together with BRN2 immunostaining in somatosensory (Rostral), parietal (Middle), and visual (Caudal) cortices (Fig. 4B,C). There was no significant genotype difference in either mean relative position of BrdU/BRN2 double-positive neurons (Fig. 4B) or mean distance from the ventricular surface (Fig. 4C). Similarly, there were no significant differences in the number of E16.5-BrdU-labeled cells, BRN2-positive cells, and BrdU/BRN2 double-positive cells in a 200- μm -wide region from the layers 1–2 boundary to the ventricular surface between wild-type and heterozygous *yotari* mice (Extended Data Fig. 4-1).

Collectively, these results confirmed that a reduction in *Dab1* gene expression does not severely disrupt the basic layer structure or layer-specific spatial distribution of neocortical neurons. In addition, these findings suggest that expression from a single *Dab1* gene is sufficient for the radial migration of late-born neurons, and that the reduction in layer 1 thickness is not caused by disruption of radial migration of the neocortical neurons.

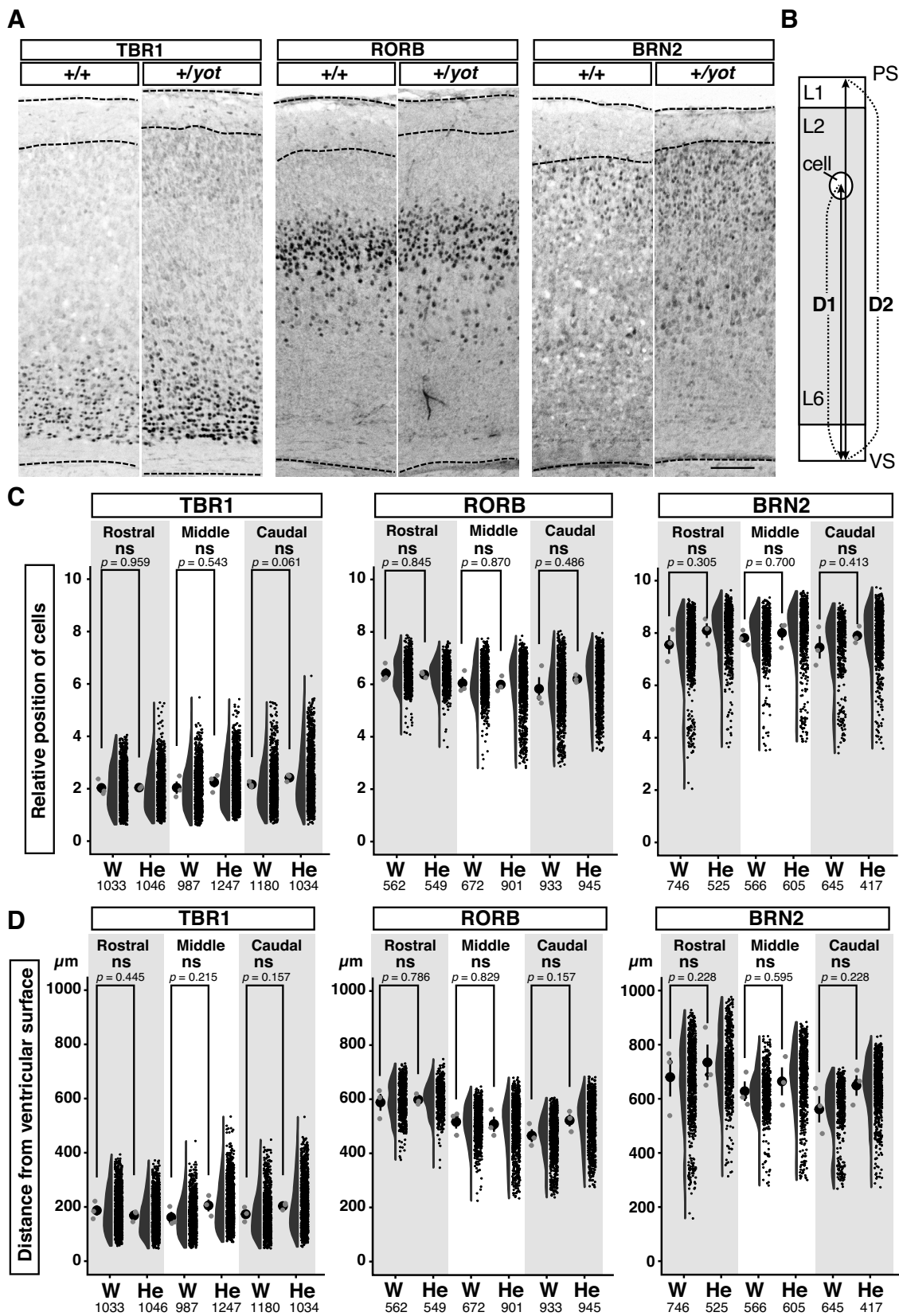


Figure 3. Half reduction of the *Dab1* gene dosage does not cause a significant positional change of neocortical layer 2–6 neurons. **A**, TBR1-positive, RORB-positive, or BRN2-positive cells in the somatosensory (Rostral), parietal (Middle), and visual (Caudal) cortices of P7 wild-type (+/+) and heterozygous *yotari* mice (+/*yot*). Representative images of coronal neocortical sections in the middle

continued

brain region are shown. **B**, Schematic illustration showing a region of the cerebral neocortex. Distances from the ventricular surface (VS) to the target cells (D1) and cortical wall thickness (D2) were measured, and the relative positions of cells were calculated by dividing D1 by D2 and multiplying by 10. **C, D**, Combination of dot, violin, and scatter plots showing the relative positions of layer marker-positive cells (**C**) and distances of layer marker-positive cells from the ventricular surface (**D**) within three brain regions along the rostro-caudal axis. The black dot and bar in the leftmost dot plot indicate the mean and SD, respectively, and each gray dot indicates the mean of one brain. Each black circle in the scatter plot is a raw datapoint. Measurements were performed on three brains from different litters ($n = 3$) per group. The total number of analyzed cells (pooled from three mice per group) are shown below each graph. After calculation of mean values for each brain, most group differences were analyzed by independent samples Student's t test; however, some experiments were analyzed by Mann-Whitney U test [**C**, BRN2 (Middle)] or unpaired Welch's t test [**C**, TBR1 (Rostral); **D**, TBR1 (Rostral)]. The p -values are labeled on the graph. ns (not significant) $p > 0.05$. Scale bar: 100 μm .

Abnormal splitting of the CA1 pyramidal layer in heterozygous *yotari* mice is caused mainly by migration failure of late-born neurons

Nissl staining revealed an abnormally split CA1 cell layer in the caudal hippocampus of P7 heterozygous *yotari* mice (Fig. 1C,C'). To investigate the identity of the abnormally located cells and to determine their birthdates, mice were injected with BrdU at E12.5, E14.5, and E16.5, and brains were fixed for co-staining with the CA1 neurons marker CTIP2 at P9 (Fig. 5A). Subsequent analysis revealed that almost all abnormally located cells were CTIP2-positive and most were produced in the late stages of development as shown by greater BrdU staining at E16.5 compared with earlier times (Fig. 5A,B).

We then examined whether splitting of the CTIP2-positive pyramidal cell layer is caused by failure of neuronal migration. According to the GFP-labeling study, E16.5-born neurons labeled with GFP by *in utero* electroporation migrate within the stratum oriens (SO) around P0–P3 and reach the top of the pyramidal cell layer at P4 (Kitazawa et al., 2014). Thus, we examined the positioning of E16.5 BrdU-labeled and CTIP2-positive cells at P3. We found that more E16.5 BrdU-labeled CTIP2-positive cells were distributed in the SO of heterozygous *yotari* mice than wild-type mice at P3 (Fig. 5D). These results suggest that abnormal splitting of the pyramidal cell layer occurs during migration within the SO and is already started at P3 (region shown with brackets in Fig. 5C +/yot).

Mispositioned hippocampal pyramidal neurons in heterozygous *yotari* mice have shorter and misoriented apical dendrites

Previous studies have shown that null mutation of the *Dab1* gene impairs pyramidal neuron development and reduces dendritic complexity in the hippocampus (Niu et al., 2004; Matsuki et al., 2008). Here, we examined whether reduced *Dab1* also results in abnormal apical dendrite morphology by sparse *in utero* labeling of hippocampal pyramidal neurons using a DIO reporter system (Sohal et al., 2009; Fig. 6A). Briefly, a reporter gene (GFP or mCherry) is inserted within the DIO cassette in reverse orientation with respect to the promoter, thereby preventing translation under normal conditions but allowing translation in the presence of Cre recombinase as the reporter gene orientation is switched. Further, to induce DIO-mediated reporter gene expression specifically in neurons, Cre expression was controlled by a promoter for *Doublecortin* (*Dcx*), a gene thought to be

expressed predominantly in newly generated neurons, including hippocampal pyramidal neurons (X. Wang et al., 2007; Yoo et al., 2011). Thus, we co-injected rAAV vectors carrying (1) a Cre recombinase driven by a *Dcx* promoter (AAV-DCX-Cre), (2) DIO-EGFP driven by a CAG promoter (AAV-CAG-DIO-EGFP), or (3) DIO-mCherry driven by a CAG promoter (AAV-CAG-DIO-mCherry) to wild-type and heterozygous *yotari* mice at P0, and prepared brain sections at P7. For sparse labeling, concentrations of AAV-CAG-DIO-EGFP and AAV-CAG-DIO-mCherry were appropriately reduced based on prior examinations. We then compared apical dendrite morphology among (1) mCherry-positive cells distributed within the pyramidal cell layer of wild-type mice (Fig. 6B–C'), (2) mCherry-positive cells normally distributed within the pyramidal cell layer of heterozygous *yotari* mice (Fig. 6E,E', yellow arrowheads), and (3) mCherry-positive cells ectopically distributed within the SO of heterozygous *yotari* mice (Fig. 6D–E', cyan arrowheads). Total apical dendrite length was significantly shorter among ectopically positioned neurons in heterozygous *yotari* mice compared with wild-types (Fig. 6F). Total apical dendritic length was also numerically reduced among normally positioned neurons in heterozygous *yotari* mice compared with wild types, although the difference did not reach statistical significance. In addition, the total number of branching points was numerically reduced among normally positioned and ectopically positioned neurons of heterozygous *yotari* mice compared with wild-types (Fig. 6G). Furthermore, many of the primary apical dendrites in ectopically positioned neurons of heterozygous *yotari* mice were orientated in abnormal directions, although the average did not differ significantly between genotypes (Fig. 6H).

Neocortical layer 2 pyramidal neurons in heterozygous *yotari* mice tend to extend their apical dendrites within layer 2 rather than in layer 1

In addition to a migration defect, null mutation, or knock-down of *Dab1* causes hypomorphic growth and misorientation of apical dendrites in the cerebral neocortex (Niu et al., 2004; Olson et al., 2006; Franco et al., 2011). Layer 1 is composed mainly of the apical dendrites projecting from pyramidal neurons in layers 2/3 and 5, suggesting that the thinner layer 1 documented here may stem from fewer apical dendrites reaching into the superficial cortex. To simultaneously observe positioning of neurons and the fine dendritic morphology, we introduced

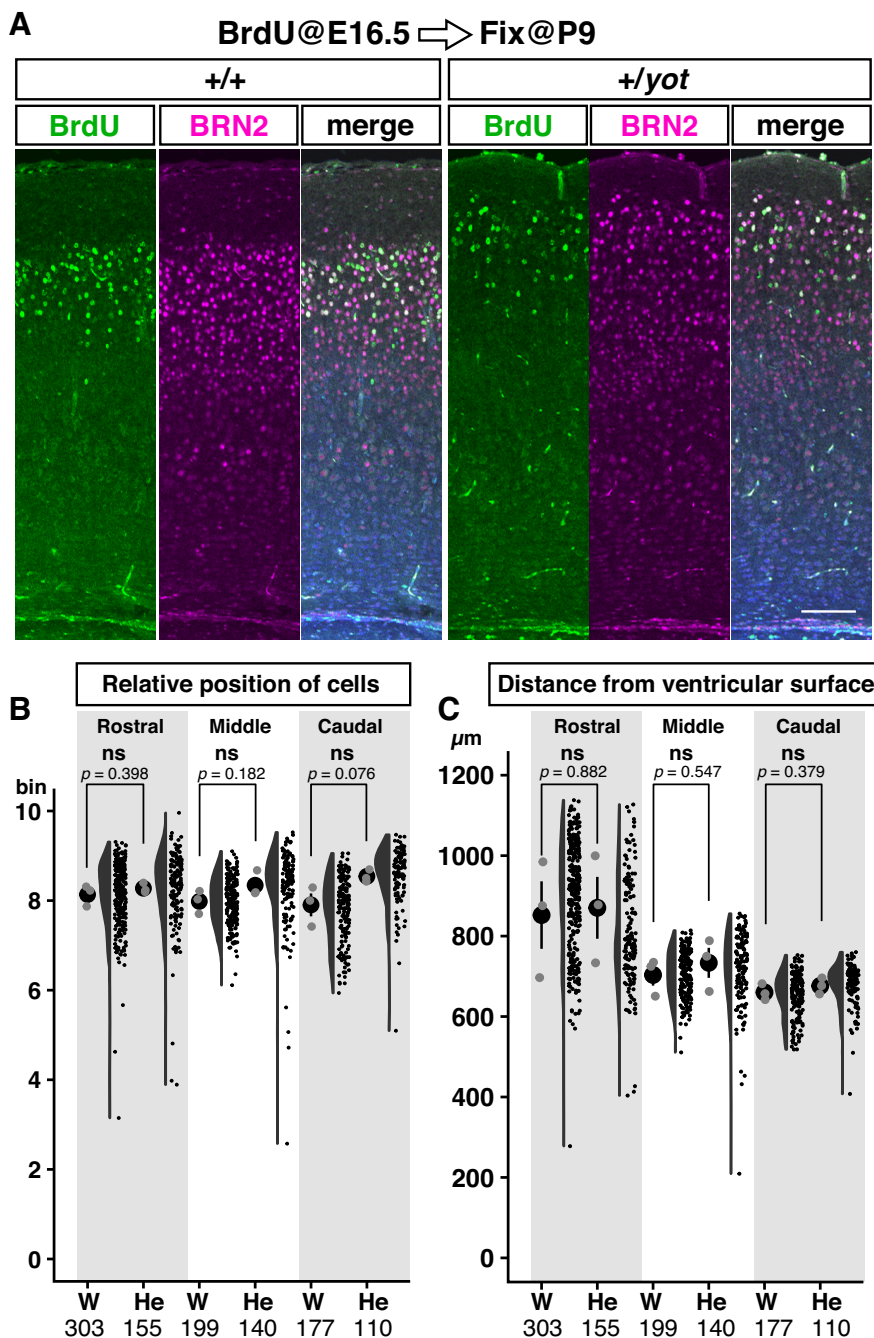


Figure 4. There were no significant positional changes in late-born, BRN2-positive, superficial neocortical neurons in *yotari* heterozygous mice. **A**, Coronal sections of P9 parietal neocortex from wild-type (+/+) and heterozygous *yotari* (+/yot) mice injected with BrdU at E16.5. Sections were co-stained with BrdU (green), the layer 2 marker BRN2 (magenta), and the nuclear stain DAPI (blue). **B**, **C**, Combination of dot, violin, and scatter plots showing relative positions of BrdU/BRN2 double-positive cells between the ventricular surface and pial surface (**B**) and distances of BrdU/BRN2 double-positive cells from the ventricular surface (**C**) in somatosensory (Rostral), parietal (Middle), and visual (Caudal) cortices of wild-type (W) and heterozygous *yotari* (He) mice. The black dot and bar in the leftmost dot plot indicate the mean and SD, respectively, each gray dot indicates the mean from one brain, and each black circle in the scatter plot is a raw datapoint. Data were obtained from three brains per group, each from different litters ($n = 3$). Total analyzed cell numbers pooled from three mice per group are shown below each graph. After calculation of the mean values for each brain, group differences were analyzed by independent samples Student's *t* test. The *p*-values are labeled on the graph. ns (not significant). Scale bar: 100 μm .

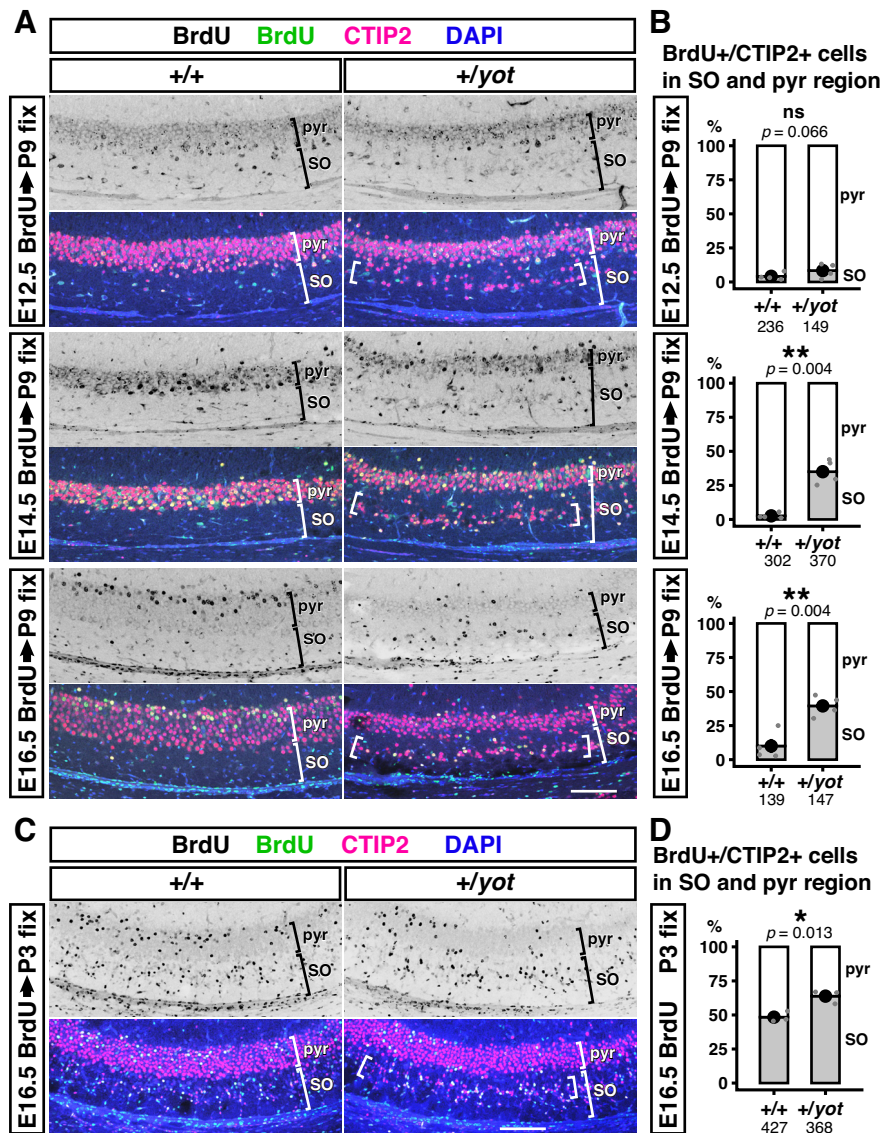


Figure 5. Abnormal splitting of the CA1 pyramidal cell layer in the caudal hippocampus of heterozygous *yotari* mice is due mainly to migration failure of later-born neurons. **A, C**, BrdU was administered at E12.5, E14.5, or E16.5 to wild-type (+/+) and heterozygous *yotari* (+/yot) mice, and brains were fixed at P9 (**A**) or P3 (**C**). Coronal sections of the caudal brain region containing the visual and auditory cortex were stained using anti-BrdU antibody (black or green) and anti-CTIP2 antibody (magenta), while nuclei were stained with DAPI (blue). Abnormal splitting of the CA1 pyramidal cell layer is indicated by the region between two brackets in stratum oriens. SO, stratum oriens; pyr, pyramidal cell layer. **B, D**, Proportions (%) of BrdU/CTIP2 double-positive cells within the SO and pyramidal cell layer (pyr) shown by 100% stacked bar chart and dot plots. The black dots within the bar indicate the mean percentage of four (**B**) or three (**D**) brains from different litters ($n = 4$ or 3), and the SD is shown by the black bars. Each gray dot indicates the mean from one brain. The number of analyzed cells is shown below each graph. After calculation of mean values from each brain, group differences were analyzed by independent samples Student's *t* test (**B**, BrdU labeling at E12.5 in the wild-type vs heterozygote, BrdU labeling at E16.5 in the wild-type vs heterozygote, and **D**) or Welch's unpaired *t* test (**B**, BrdU labeling at E14.5 in the wild-type vs heterozygote). The *p*-values are labeled on the graph. * $p < 0.05$, ** $p < 0.01$, ns (not significant) $p > 0.05$. Scale bar: 100 μm .

a plasmid DNA solution containing pCAGGS-RG, which expresses DsRed under the control of a CAG promoter, and pDCX-Cre into late-born superficial neurons by *in utero* electroporation at E16.5 (Fig. 7A). Since the DsRed cassette is flanked by two loxP sites, in the presence of Cre, the DsRed cassette is removed and EGFP begins to be transcribed. By reducing the concentration of pDCX-

Cre, we sparsely labeled neurons with EGFP. For quantitative analysis of apical dendrite morphology, we first measured the angle between the first branch point (the end of the main shaft of the apical dendrite) and the perpendicular line passing through the center of the cell body (Fig. 7D,E) but found no significant difference between genotypes (Fig. 7E). Similarly, there were no genotype

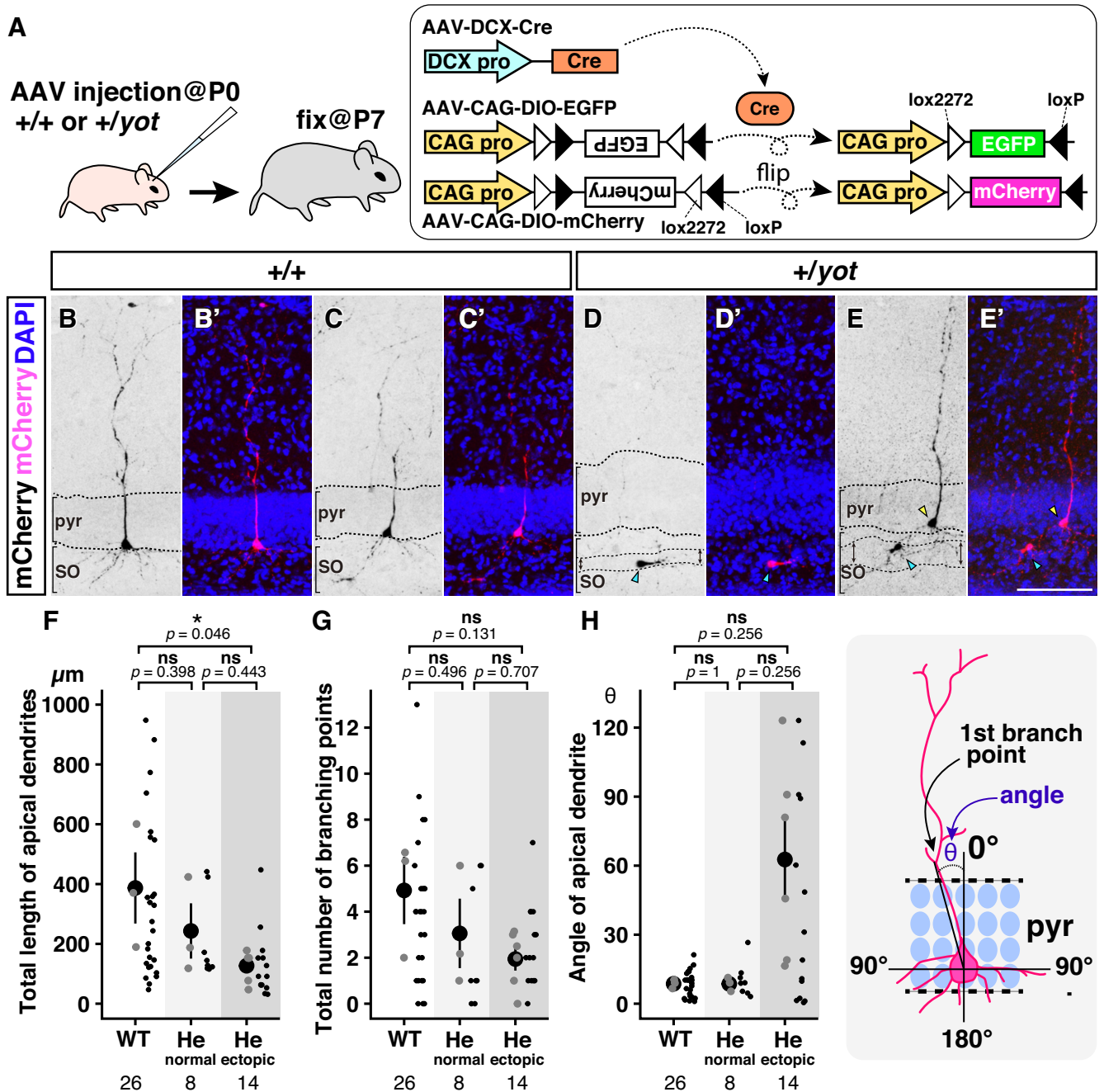


Figure 6. Ectopic cells within the split pyramidal cell layer have shorter and misoriented apical dendrites. **A**, Schematic illustration showing the time schedule and strategy for sparse labeling of hippocampal cells. A mixture of AAV-DCX-Cre, AAV-CAG-DIO-EGFP, and AAV-CAG-DIO-mCherry was injected into the lateral ventricles of wild-type and heterozygous *yotari* mice at P0, and brain slices were prepared at P7. AAV-DCX-Cre expresses Cre under the control of a DCX promoter (DCX pro), while AAV-CAG-DIO-EGFP and AAV-CAG-DIO-mCherry contain a DIO-EGFP or DIO-mCherry cassette driven by a CAG promoter (CAG pro). The DIO cassette is composed of two reciprocally oriented loxP sites (black triangles) and two lox2272 sites (white triangles), and EGFP, or mCherry cDNA was inserted within the DIO cassette in the opposite direction to the CAG promoter; therefore, there is no transcription of those cDNA under normal conditions. However, simultaneous infection with Cre recombinase flips the orientation of EGFP or mCherry cDNA into the forward direction by two-step recombination between loxP and lox2272 sites. The enclosed rectangle and rounded rectangle represent the Cre cDNA and Cre protein, respectively. **B–E'**, Coronal sections of caudal neocortex (including visual and auditory cortex) from wild-type (+/+, **B–C'**) and heterozygous *yotari* (+/-yot, **D–E'**) mice were stained with anti-RFP (black or magenta) and DAPI (blue). Representative images of mCherry-positive cells in the pyramidal cell layer (pyr) of wild-type mice (**B–C'**), normally distributed cells in the pyramidal cell layer of heterozygous *yotari* mice (yellow arrowheads in **E** and **E'**), and ectopically distributed cells in the SO (cyan arrowheads in **D–E'**) of heterozygous *yotari* mice (**D–E'**). The ectopic cell regions in the SO of heterozygous *yotari* mice are indicated by double-headed arrows (**D** and **E**). **F–H**, Total length of apical dendrites (**F**), total number of

continued

branching points (**G**), and angle of apical dendrites (**H**) obtained for 26 neurons from three wild-type (WT) mice, eight normally distributed neurons from three heterozygous *yotari* mice (He, normal), and 14 ectopically distributed neurons from six heterozygous *yotari* mice (He, ectopic) are plotted by a combination of dot and scatter plots. All analyzed mice were obtained from different litters. The large black dot and the bar in the leftmost dot plot indicate the mean and SD, respectively, and the gray dots indicate the mean from one brain. Each small black dot in the scatter plot is a raw datapoint. The total number of analyzed cells is shown below each graph. After calculation of the mean values from each brain, groups were compared by Tukey–Kramer test (**F** and **G**) or Steel–Dwass test (**H**). The *p*-values are labeled on the graph. **p* < 0.05, ns (not significant) *p* > 0.05. The schematic drawing in H shows a pyramidal neuron in the pyramidal cell layer (pyr). The angle (θ) of the primary apical dendrite was determined as the angle between a perpendicular line passing through the center of the neuron and the first branch point.

differences in total length and total number of branching points (Fig. 7F,H). However, we found significant differences both in the total length of apical dendrites and the total number of branching points when measured separately within layers 1 and 2 (Fig. 7G,I). Those apical dendrites within layer 1 were significantly shorter and less morphologically complex in heterozygous *yotari* mutant mice than wild-type mice, while those within layer 2 were longer and more branched in heterozygous *yotari* mutant mice. These results suggest that a reduction of DAB1 protein disrupts the normal guidance of apical dendrites.

Discussion

We demonstrate that *Dab1* is haploinsufficient for the formation of the cerebral neocortex and hippocampus, although specific developmental processes are differentially sensitive to *Dab1* gene dose. Neocortical layer 1 is thinner in heterozygous *yotari* mutant mice than in wild-type mice (Figs. 1 and 2), but layer marker staining and BrdU birth-dating indicated that half reduction of *Dab1* does not disrupt radial neuronal migration and layer formation (Figs. 3 and 4). Rather, sparse labeling revealed that layer 2 neurons tend to elongate apical dendrites within layer 2 rather than layer 1 (Fig. 7). Heterozygous *yotari* mutant mice also exhibit splitting of the CA1 pyramidal cell layer in the caudal hippocampus (Figs. 1 and 5), and BrdU birth-dating studies suggests that this developmental abnormality is caused, at least in part, by migration defects of late-born pyramidal neurons (Fig. 5). Further, sparse labeling revealed that mispositioned neurons in the SO tend to have short and abnormally orientated dendrites (Fig. 6). Thus, reduction of *Dab1* gene expression has distinct effects on development of the cerebral neocortex and hippocampus.

Homozygous null mutation of the *Dab1* gene causes severe migration failure both in the cerebral neocortex and hippocampus (Howell et al., 1997; Yoneshima et al., 1997; Franco et al., 2011; Blume et al., 2017). However, half reduction of *Dab1* gene expression did not cause migration failure in the cerebral neocortex, and impaired only late-born pyramidal neuron migration in the caudal hippocampus. This regional difference may be attributable to distinct migration modes. Early-born pyramidal neurons in the cerebral neocortex migrate radially by somal translocation, while late-born neurons follow a series of steps including multipolar migration, locomotion, and terminal translocation (Noctor et al., 2001; Tabata and Nakajima, 2003; Tabata et al., 2009; Sekine et al., 2011; Ohtaka-Maruyama and Okado, 2015; Kon et al.,

2017). In contrast, hippocampal pyramidal neurons migrate radially by a climbing mode after a multipolar stage (Kitazawa et al., 2014; Hayashi et al., 2015). These various migration modes may have different DAB1 protein sensitivities (requirements), although it is still unclear why only the caudal hippocampus is affected as migration modes are similar across the hippocampal rostral–caudal axis. It may be that a subpopulation of pyramidal neurons in caudal hippocampus, possibly comprising a specific sublayer, requires both *Dab1* gene copies for proper migration in the caudal hippocampus (Soltész and Losonczy, 2018).

Homozygous null mutation of the *Dab1* gene also causes complete loss of cerebral neocortex layer 1 (Sweet et al., 1996; Howell et al., 1997; Ware et al., 1997; Yoneshima et al., 1997). In contrast to this severe phenotype, half reduction of *Dab1* gene resulted only in a thinner layer 1 throughout the rostral–caudal axis (Figs. 1 and 2). This abnormality appears to arise after radial neuronal migration is complete, as no obvious anatomic change in neocortical structure was observed at P0 (Extended Data Fig. 1-1), migration failure was not observed (Fig. 4), and layer-specific marker staining showed no positional changes in TBR1-positive, RORB-positive, or BRN2-positive cells (Fig. 3). These effects of heterozygous *Dab1 yotari* mutation further suggest two distinct signaling pathways for excitatory neurons with differential dependencies on *Dab1* gene dosage: a less sensitive pathway for radial neuronal migration and a sensitive pathway for the control of layer 1 thickness.

Several other mutant mouse lines exhibit abnormal and ectopic positioning of cells in cortical layer 1, including *Dab1^{p45/-}* (Herrick and Cooper, 2002), *Reelin ΔC-KI* (Kohno et al., 2015), *Vldlr* KO (Hack et al., 2007; Hirota and Nakajima, 2020), *Apoer2* KO (Hirota et al., 2018), *DeltaNp73^{Cre};ROSA26^{stop-dt-a}* (de Frutos et al., 2016), *Emx1^{Cre};Wnt3a^{dt-a}* (de Frutos et al., 2016), *Emx1-Cre*; *Pcdh-γ^{1con3/fcon3}* (Garrett et al., 2012), *Plexin A2/A4* double KO (Hatanaka et al., 2019), and *Sema6a* KO (Hatanaka et al., 2019) mice. Many of these lines harbor mutations in the Reelin signaling pathway. The *Dab1^{p45}* gene encodes a hypomorphic alternative splice variant of *Dab1*, and *Dab1^{p45/-}* mice also show thinning of layer 1 and splitting of the CA1 pyramidal layer (Herrick and Cooper, 2002). Since the *Dab1^{p45}* allele was created by the insertion of *Dab1^{p45}* cDNA, only the DAB1 p45 protein is expressed in this mouse (Herrick and Cooper, 2002). Therefore, the *Dab1^{p45/-}* condition is distinct from the heterozygous null condition, and analysis of heterozygous

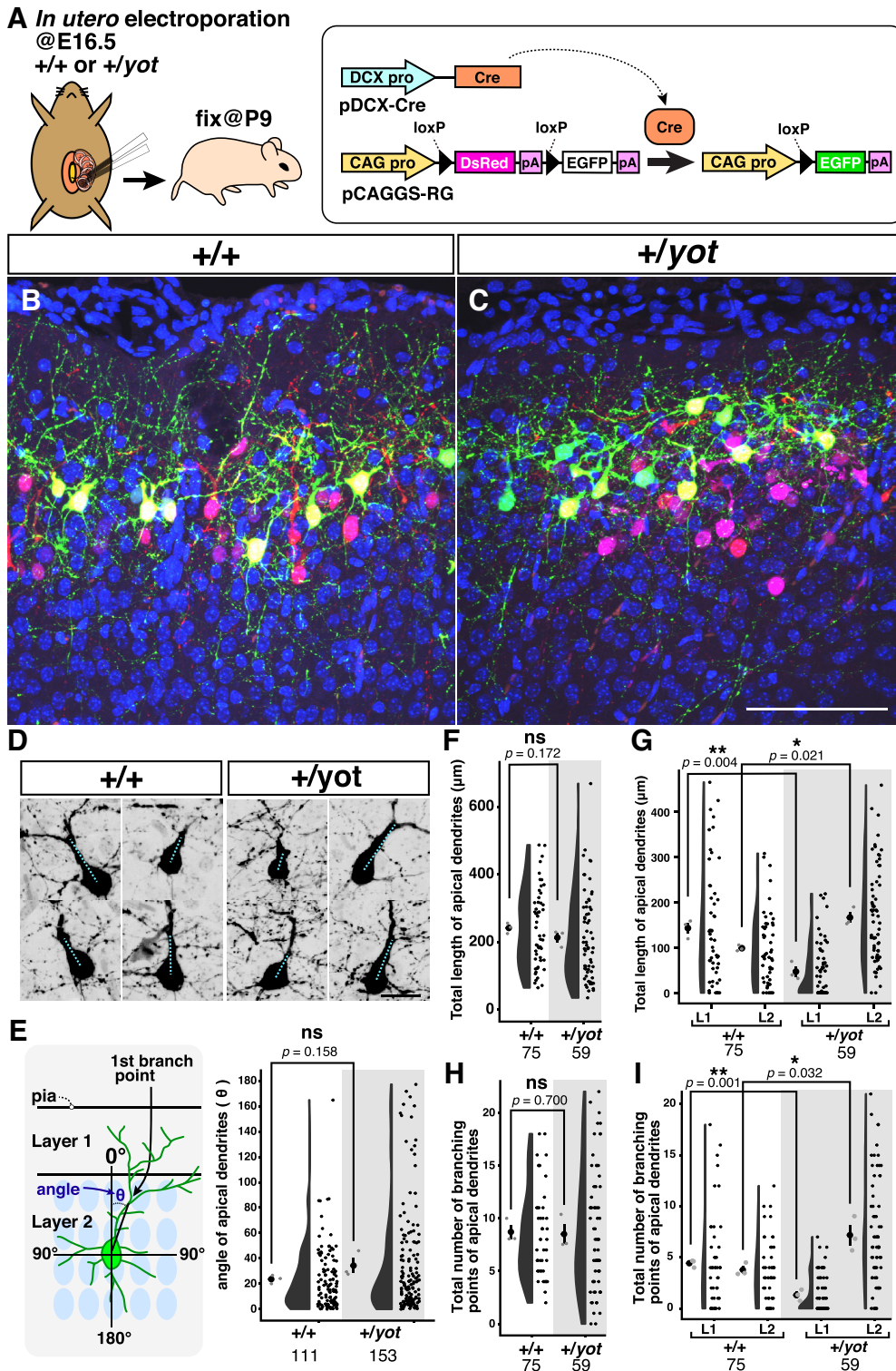


Figure 7. Superficial late-born neocortical neurons of heterozygous *yotari* mice show less apical dendrite sprouting in layer 1. **A**, Strategy and time schedule for sparse labeling of superficial neurons. The DCX promoter-driven Cre expression plasmid pDCX-Cre was co-electroporated with the Cre-reporter plasmid pCAGGS-RG at E16.5, and mice were fixed at P9. In the absence of Cre, the pCAGGS-RG expresses DsRed under the CAG promoter, whereas in the presence of Cre, the floxed-DsRed-poly A expression cassette is excised and the plasmid expresses EGFP. To reduce the recombination probability, pDCX-Cre plasmid concentration was significantly reduced. DCX pro, CAG pro, and pA represent the DCX promoter, CAG promoter, and simian virus 40 polyadenylation signal, respectively. The rectangle and rounded rectangle represent the Cre cDNA and Cre protein, respectively. **B**, **C**, Electroporated brains at P9 obtained from wild-type (**B**, +/+) and heterozygous *yotari* mice (**C**, +/yot) were sectioned coronally. The superficial part of the somatosensory cortex is shown. Scale bar: 100 μ m. **D**, Sparsely labeled EGFP-positive cells obtained

continued

from wild-type (+/+) and heterozygous *yotari* mice (+/*yot*) for measurement of primary apical dendrite angle. Cyan dotted lines are drawn from the center of the cell body to the first branch point. Scale bar: 20 μm . **E**, A schematic illustrating a neuron in the superficial cerebral neocortex. The angle of the primary apical dendrite (θ) was defined as the angle between a perpendicular line passing through the center of the cell and the first branch point. **E–G**, Combination of dot, violin, and scatter plots showing the apical dendrite angle (**E**), total length (**F**), and total lengths specifically in layer 1 (L1) and layer 2 (L2) (**G**). **H, I**, The total number of apical dendrite branching points (**H**) and the total number of branching points within layer 1 (L1) and layer 2 (L2) (**I**) obtained from three WT (+/+) and six heterozygous *yotari* mice (+/*yot*) from different litters. The black dot and bar in the leftmost dot plot indicate the mean and the SD, respectively, and the gray dots indicates the mean for each brain. Each black circle in the scatter plot is a raw data-point. The total number of analyzed cells is shown below each graph. After calculation of mean values for each brain, groups were compared by independent samples Student's *t* test (**E, F, G, I**) or Mann–Whitney *U* test (**H**). The *p*-values are labeled on the graph. **p* < 0.05, ***p* < 0.01, ns (not significant) *p* > 0.05.

Dab1 mutant mice such as *yotari* could be particularly valuable for elucidating the pathomechanisms of human diseases associated with heterozygous *Dab1* loss-of-function mutations. While it is yet unknown whether haploinsufficiency of the *Dab1* gene has similar effects on human cortical and hippocampal development, haploinsufficiency of the related *Reelin* gene is associated with various neuropsychiatric disorders (Guidotti et al., 2016; Ishii et al., 2016; Hattori and Kohno, 2021). Given the critical role of *Dab1* in the canonical Reelin signaling pathway (Honda et al., 2011; Jossin, 2020), the findings of this study could provide potential explanations for human diseases.

Similar to heterozygous *yotari* mice, *Reelin* $\Delta\text{C-KI}$ mouse lacking the C-terminal region of Reelin, which is thought to be required for efficient DAB1 phosphorylation (Nakano et al., 2007), gradually show thinning of layer 1 and apical dendrites with abnormal orientations that tend to avoid growing into the layer 1 (Kohno et al., 2015). The *DeltaNp73^{Cre};ROSA26^{stop-dt-a}* and the *Emx1^{Cre};Wnt3a^{dt-a}* mouse lines also underexpress Reelin protein and show reduced layer 1 thickness and cortical neurons with decreased apical dendrite tuft complexity (de Frutos et al., 2016). Since the Reelin receptor VLDLR is predominantly expressed in the superficial cerebral neocortex (Hirota et al., 2015), *Vldlr* KO would result in deficient Reelin signaling within superficial cortical layers, and indeed *Vldlr* KO also results in ectopic positioning of CUX1-positive or CUX2-positive neurons in layer 1 (Hack et al., 2007; Hirota and Nakajima, 2020). Therefore, it appears that partial attenuation of the Reelin–*Dab1* signaling pathway does not inhibit radial neuronal migration in the cerebral neocortex but causes a decrease in the layer 1 thickness.

We suggest that these deficits account at least in part for the reduction in layer 1 thickness. Layer 1 is composed of the apical dendrites of excitatory neurons within layers 2/3 and 5, local interneurons, and Cajal–Retzius cells, thalamic axons, and axons of excitatory neurons projecting from other layers and regions of the cerebral neocortex (Solari and Stoner, 2011; Harris and Shepherd, 2015; Genescu and Garell, 2021; Gesuita and Karayannis, 2021; Schuman et al., 2021). However, there is a particularly strong association between apical dendrites and layer 1 thickness as evidenced by (1) the tendency of apical dendrites projecting from sparsely labeled superficial layer neurons in heterozygous *yotari* mice to elongate within layer 2 but not layer 1 (Fig. 7), (2) the reduced layer 1 thickness and associated apical dendrite maldevelopment among *Reelin* C-terminal deletion mutant mice (Kohno et

al., 2015), Reelin-producing Cajal–Retzius cell-ablated mice (de Frutos et al., 2016), and *Dab1* knock-down or knock-out experiments (Olson et al., 2006; Franco et al., 2011; Sekine et al., 2011, 2012), and (3) defects in apical dendrite morphology observed in other mutants with abnormal layer 1 reduction, such as *Emx1-Cre;Pcdh- $\gamma^{\text{fcon3/fcon3}}$* (Garrett et al., 2012), *PlexinA2/A4* double KO, and *Sema6a* KO mice (Hatanaka et al., 2019). Thus, abnormalities in the apical dendrites of neocortical pyramidal neurons may explain reduced layer 1 thickness. It is also possible that the increase in cell number within other neocortical layers (Extended Data Fig. 3-1) leads to a reduction in layer 1 thickness. The causal relationship between the increase in cell number and the expansion of the neocortical area, and why the cell number increased, are important subjects for future study.

In addition to abnormal development of neocortical layer 2 apical dendrites, we also observed a decrease in the total length of apical dendrites projecting from ectopic pyramidal neurons of the caudal hippocampus as well as misoriented apical dendrites among subset of neurons. While it is possible that the half reduction of DAB1 protein directly caused these phenotypes (Niu et al., 2004; Matsuki et al., 2008), it is also possible that these abnormalities are secondary to migration failure or that neurons ectopically distributed in the SO region are still migrating and these misoriented structures are leading processes rather than dendrites. Regardless of mechanism, the resulting maldevelopment in the hippocampus may contribute to a myriad of neuropsychiatric diseases exhibiting deficits in learning and memory formation (Hainmueller and Bartos, 2020).

Similar to the *Dab1* gene, the *Reelin* gene is also known to exhibit haploinsufficiency (Liu et al., 2001; Carboni et al., 2004; Qiu et al., 2006; Nullmeier et al., 2011; Bouamrane et al., 2016; L. Wang et al., 2019), and reduced Reelin levels have been observed in the brains of patients with schizophrenia (Impagnatiello et al., 1998; Guidotti et al., 2000), bipolar disorder (Guidotti et al., 2000), autism (Fatemi et al., 2001, 2005), and Alzheimer's disease (Chin et al., 2007). Moreover, heterozygous *reeler* mice and *Reelin* $\Delta\text{C-KI}$ mice exhibit similar neurochemical, behavioral, and cognitive abnormalities to those observed in autism or schizophrenia (Costa et al., 2001; Tremolizzo et al., 2002; Carboni et al., 2004; Nullmeier et al., 2011; Sakai et al., 2016; Sánchez-Hidalgo et al., 2022). The anatomic abnormalities we observed in heterozygous *yotari* mice may also be related to behavioral defects because

layer 1 and hippocampus are essential for higher-order cognitive functions (Hainmueller and Bartos, 2020; Schuman et al., 2021). Consistent with this possibility, behavioral abnormalities observed in schizophrenia, such as hyperactivity, decreased anxiety-like behavior, and impaired working memory, have been observed in dorsal forebrain-specific *Dab1* conditional knock-out mice (Imai et al., 2017). These findings suggest that therapeutic enhancement of Reelin signaling could prevent or ameliorate the cognitive deficits of schizophrenia and other neurodevelopmental disorders (Guidotti et al., 2016; Ishii et al., 2016; Hattori and Kohno, 2021). Indeed, administration of Reelin to mouse models of cognitive dysfunction such as Angelman syndrome and schizophrenia could prevent or ameliorate the cognitive deficits. (Hethorn et al., 2015; Ishii et al., 2015; Ibi et al., 2020; Sawahata et al., 2021). If a similar neuropsychiatric abnormality is observed because of *Dab1* haploinsufficiency, it may be possible to ameliorate the defect by activating the *Dab1* signaling through Reelin supplementation.

In conclusion, while the radial migration of neocortical neurons can proceed normally when *Dab1* is reduced to half, *Dab1* is haploinsufficient for maintaining layer 1 thickness and for the migration of late-born pyramidal neurons in the caudal hippocampus. Further studies are required to explore why these developmental events are differentially dependent on *Dab1* expression level. We suggest that elucidation of the Reelin signaling pathways may provide clues to neuropsychiatric disease pathogenesis and potential therapeutic strategies.

References

- Assadi AH, Zhang G, Beffert U, McNeil RS, Renfro AL, Niu S, Quattrocchi CC, Antalffy BA, Sheldon M, Armstrong DD, Wynshaw-Boris A, Herz J, D'Arcangelo G, Clark GD (2003) Interaction of reelin signaling and Lis1 in brain development. *Nat Genet* 35:270–276.
- Ballif BA, Arnaud L, Arthur WT, Guris D, Imamoto A, Cooper JA (2004) Activation of a *Dab1/CrkL/C3G/Rap1* pathway in Reelin-stimulated neurons. *Curr Biol* 14:606–610.
- Bar I, Lambert De Rouvroit C, Royaux I, Krizman DB, Dérnoncourt C, Ruelle D, Beckers MC, Goffinet AM (1995) A YAC contig containing the reeler locus with preliminary characterization of candidate gene fragments. *Genomics* 26:543–549.
- Blume M, Inoguchi F, Sugiyama T, Owada Y, Osumi N, Aimi Y, Taki K, Katsuyama Y (2017) *Dab1* contributes differently to the morphogenesis of the hippocampal subdivisions. *Dev Growth Differ* 59:657–673.
- Bock HH, Jossin Y, Liu P, Förster E, May P, Goffinet AM, Herz J (2003) Phosphatidylinositol 3-kinase interacts with the adaptor protein *Dab1* in response to Reelin signaling and is required for normal cortical lamination. *J Biol Chem* 278:38772–38779.
- Bouamrane L, Scheyer AF, Lassalle O, Iafrafi J, Thomazeau A, Chavis P (2016) Reelin-haploinsufficiency disrupts the developmental trajectory of the E/I balance in the prefrontal cortex. *Front Cell Neurosci* 10:308.
- Burger C, Nash KR (2016) Small-scale recombinant adeno-associated virus purification. *Methods Mol Biol* 1382:95–106.
- Carboni G, Tueting P, Tremolizzo L, Sugaya I, Davis J, Costa E, Guidotti A (2004) Enhanced dizocilpine efficacy in heterozygous reeler mice relates to GABA turnover downregulation. *Neuropharmacology* 46:1070–1081.
- Caviness VS Jr (1982) Neocortical histogenesis in normal and reeler mice: a developmental study based upon [3H]thymidine autoradiography. *Brain Res* 256:293–302.
- Chen K, Ochalski PG, Tran TS, Sahir N, Schubert M, Pramatarova A, Howell BW (2004) Interaction between *Dab1* and *Crkl* is promoted by Reelin signaling. *J Cell Sci* 117:4527–4536.
- Chin J, Massaro CM, Palop JJ, Thwin MT, Yu GQ, Bien-Ly N, Bender A, Mucke L (2007) Reelin depletion in the entorhinal cortex of human amyloid precursor protein transgenic mice and humans with Alzheimer's disease. *J Neurosci* 27:2727–2733.
- Cooper JA (2008) A mechanism for inside-out lamination in the neocortex. *Trends Neurosci* 31:113–119.
- Costa E, Davis J, Grayson DR, Guidotti A, Pappas GD, Pesold C (2001) Dendritic spine hypoplasticity and downregulation of reelin and GABAergic tone in schizophrenia vulnerability. *Neurobiol Dis* 8:723–742.
- D'Arcangelo G (2005) The reeler mouse: anatomy of a mutant. *Int Rev Neurobiol* 71:383–417.
- D'Arcangelo G, Miao GG, Chen SC, Soares HD, Morgan JI, Curran T (1995) A protein related to extracellular matrix proteins deleted in the mouse mutant reeler. *Nature* 374:719–723.
- D'Arcangelo G, Homayouni R, Keshvara L, Rice DS, Sheldon M, Curran T (1999) Reelin is a ligand for lipoprotein receptors. *Neuron* 24:471–479.
- de Frutos CA, Bouvier G, Arai Y, Thion MS, Lokmane L, Keita M, Garcia-Dominguez M, Charnay P, Hirata T, Riethmacher D, Grove EA, Tissir F, Casado M, Pierani A, Garel S (2016) Reallocation of olfactory Cajal-Retzius cells shapes neocortex architecture. *Neuron* 92:435–448.
- Falconer DS (1951) Two new mutants, 'trembler' and 'reeler', with neurological actions in the house mouse (*Mus musculus* L.). *J Genet* 50:192–201.
- Fatemi SH, Stary JM, Halt AR, Realmuto GR (2001) Dysregulation of Reelin and Bcl-2 proteins in autistic cerebellum. *J Autism Dev Disord* 31:529–535.
- Fatemi SH, Snow AV, Stary JM, Araghi-Niknam M, Reutiman TJ, Lee S, Brooks AI, Pearce DA (2005) Reelin signaling is impaired in autism. *Biol Psychiatry* 57:777–787.
- Feng L, Allen NS, Simo S, Cooper JA (2007) Cullin 5 regulates *Dab1* protein levels and neuron positioning during cortical development. *Genes Dev* 21:2717–2730.
- Franco SJ, Martinez-Garay I, Gil-Sanz C, Harkins-Perry SR, Müller U (2011) Reelin regulates cadherin function via *Dab1/Rap1* to control neuronal migration and lamination in the neocortex. *Neuron* 69:482–497.
- Garrett AM, Schreiner D, Lobas MA, Weiner JA (2012) γ -Protocadherins control cortical dendrite arborization by regulating the activity of a FAK/PKC/MARCKS signaling pathway. *Neuron* 74:269–276.
- Genescu I, Garel S (2021) Being superficial: a developmental viewpoint on cortical layer 1 wiring. *Curr Opin Neurobiol* 66:125–134.
- Gesuita L, Karayannis T (2021) A 'marginal' tale: the development of the neocortical layer 1. *Curr Opin Neurobiol* 66:37–47.
- Guidotti A, Auta J, Davis JM, Di-Giorgi-Gerevini V, Dwivedi Y, Grayson DR, Impagnatiello F, Pandey G, Pesold C, Sharma R, Uzunov D, Costa E (2000) Decrease in reelin and glutamic acid decarboxylase67 (*GAD67*) expression in schizophrenia and bipolar disorder: a postmortem brain study. *Arch Gen Psychiatry* 57:1061–1069.
- Guidotti A, Grayson DR, Caruncho HJ (2016) Epigenetic RELN dysfunction in schizophrenia and related neuropsychiatric disorders. *Front Cell Neurosci* 10:89.
- Hack I, Hellwig S, Junghans D, Brunne B, Bock HH, Zhao S, Frotscher M (2007) Divergent roles of ApoER2 and Vldlr in the migration of cortical neurons. *Development* 134:3883–3891.
- Hainmueller T, Bartos M (2020) Dentate gyrus circuits for encoding, retrieval and discrimination of episodic memories. *Nat Rev Neurosci* 21:153–168.
- Hamburg M (1963) Analysis of the postnatal developmental effects of "Reeler," a neurological mutation in mice. A study in developmental genetics. *Dev Biol* 8:165–185.

- Harris KD, Shepherd GM (2015) The neocortical circuit: themes and variations. *Nat Neurosci* 18:170–181.
- Hatanaka Y, Kawasaki T, Abe T, Shioi G, Kohno T, Hattori M, Sakakibara A, Kawaguchi Y, Hirata T (2019) Semaphorin 6A-Plexin A2/A4 interactions with radial glia regulate migration termination of superficial layer cortical neurons. *iScience* 21:359–374.
- Hattori M, Kohno T (2021) Regulation of Reelin functions by specific proteolytic processing in the brain. *J Biochem* 169:511–516.
- Hayashi K, Kubo K, Kitazawa A, Nakajima K (2015) Cellular dynamics of neuronal migration in the hippocampus. *Front Neurosci* 9:135.
- Herrick TM, Cooper JA (2002) A hypomorphic allele of *dab1* reveals regional differences in reelin-Dab1 signaling during brain development. *Development* 129:787–796.
- Hethorn WR, Ciarlone SL, Filonova I, Rogers JT, Aguirre D, Ramirez RA, Grieco JC, Peters MM, Gulick D, Anderson AE, J LB, Lussier AL, Weeber EJ (2015) Reelin supplementation recovers synaptic plasticity and cognitive deficits in a mouse model for Angelman syndrome. *Eur J Neurosci* 41:1372–1380.
- Hiesberger T, Trommsdorff M, Howell BW, Goffinet A, Mumby MC, Cooper JA, Herz J (1999) Direct binding of Reelin to VLDL receptor and ApoE receptor 2 induces tyrosine phosphorylation of disabled-1 and modulates tau phosphorylation. *Neuron* 24:481–489.
- Hirota Y, Nakajima K (2020) VLDLR is not essential for reelin-induced neuronal aggregation but suppresses neuronal invasion into the marginal zone. *Development* 147:dev189936.
- Hirota Y, Kubo K, Katayama K, Honda T, Fujino T, Yamamoto TT, Nakajima K (2015) Reelin receptors ApoER2 and VLDLR are expressed in distinct spatiotemporal patterns in developing mouse cerebral cortex. *J Comp Neurol* 523:463–478.
- Hirota Y, Kubo KI, Fujino T, Yamamoto TT, Nakajima K (2018) ApoER2 controls not only neuronal migration in the intermediate zone but also termination of migration in the developing cerebral cortex. *Cereb Cortex* 28:223–235.
- Hirotsune S, Takahara T, Sasaki N, Hirose K, Yoshiki A, Ohashi T, Kusakabe M, Murakami Y, Muramatsu M, Watanabe S, Nakao K, Katsuki M, Hayashizaki Y (1995) The reeler gene encodes a protein with an EGF-like motif expressed by pioneer neurons. *Nat Genet* 10:77–83.
- Honda T, Nakajima K (2006) Mouse Disabled1 (DAB1) is a nucleocytoplasmic shuttling protein. *J Biol Chem* 281:38951–38965.
- Honda T, Nakajima K (2016) Proper level of cytosolic disabled-1, which is regulated by dual nuclear translocation pathways, is important for cortical neuronal migration. *Cereb Cortex* 26:3219–3236.
- Honda T, Kobayashi K, Mikoshiba K, Nakajima K (2011) Regulation of cortical neuron migration by the Reelin signaling pathway. *Neurochem Res* 36:1270–1279.
- Howell BW, Hawkes R, Soriano P, Cooper JA (1997) Neuronal position in the developing brain is regulated by mouse disabled-1. *Nature* 389:733–737.
- Howell BW, Herrick TM, Hildebrand JD, Zhang Y, Cooper JA (2000) *Dab1* tyrosine phosphorylation sites relay positional signals during mouse brain development. *Curr Biol* 10:877–885.
- Huang Y, Magdaleno S, Hopkins R, Slaughter C, Curran T, Keshvara L (2004) Tyrosine phosphorylated Disabled 1 recruits Crk family adapter proteins. *Biochem Biophys Res Commun* 318:204–212.
- Ibi D, Nakasai G, Koide N, Sawahata M, Kohno T, Takaba R, Nagai T, Hattori M, Nabeshima T, Yamada K, Hiramatsu M (2020) Reelin supplementation into the hippocampus rescues abnormal behavior in a mouse model of neurodevelopmental disorders. *Front Cell Neurosci* 14:285.
- Imai H, Shoji H, Ogata M, Kagawa Y, Owada Y, Miyakawa T, Sakimura K, Terashima T, Katsuyama Y (2017) Dorsal forebrain-specific deficiency of reelin-Dab1 signal causes behavioral abnormalities related to psychiatric disorders. *Cereb Cortex* 27:3485–3501.
- Impagnatiello F, Guidotti AR, Pesold C, Dwivedi Y, Caruncho H, Pisu MG, Uzunov DP, Smalheiser NR, Davis JM, Pandey GN, Pappas GD, Tueting P, Sharma RP, Costa E (1998) A decrease of reelin expression as a putative vulnerability factor in schizophrenia. *Proc Natl Acad Sci U S A* 95:15718–15723.
- Ishii K, Nagai T, Hirota Y, Noda M, Nabeshima T, Yamada K, Kubo K, Nakajima K (2015) Reelin has a preventive effect on phencyclidine-induced cognitive and sensory-motor gating deficits. *Neurosci Res* 96:30–36.
- Ishii K, Kubo KI, Nakajima K (2016) Reelin and neuropsychiatric disorders. *Front Cell Neurosci* 10:229.
- Jossin Y (2020) Reelin functions, mechanisms of action and signaling pathways during brain development and maturation. *Biomolecules* 10:964.
- Jossin Y, Cooper JA (2011) Reelin, Rap1 and N-cadherin orient the migration of multipolar neurons in the developing neocortex. *Nat Neurosci* 14:697–703.
- Kitazawa A, Kubo K, Hayashi K, Matsunaga Y, Ishii K, Nakajima K (2014) Hippocampal pyramidal neurons switch from a multipolar migration mode to a novel “climbing” migration mode during development. *J Neurosci* 34:1115–1126.
- Kohno T, Honda T, Kubo K, Nakano Y, Tsuchiya A, Murakami T, Banno H, Nakajima K, Hattori M (2015) Importance of Reelin C-terminal region in the development and maintenance of the postnatal cerebral cortex and its regulation by specific proteolysis. *J Neurosci* 35:4776–4787.
- Kojima T, Nakajima K, Mikoshiba K (2000) The disabled 1 gene is disrupted by a replacement with L1 fragment in *yotari* mice. *Brain Res Mol Brain Res* 75:121–127.
- Kon E, Cossard A, Jossin Y (2017) Neuronal polarity in the embryonic mammalian cerebral cortex. *Front Cell Neurosci* 11:163.
- Kondrashov FA, Koonin EV (2004) A common framework for understanding the origin of genetic dominance and evolutionary fates of gene duplications. *Trends Genet* 20:287–290.
- Koresawa Y, Miyagawa S, Ikawa M, Matsunami K, Yamada M, Okabe M, Shirakura R (2000) A new Cre recombinase gene based on optimal codon usage in mammals: a powerful material for organ-specific gene targeting. *Transplant Proc* 32:2516–2517.
- Liu WS, Pesold C, Rodriguez MA, Carboni G, Auta J, Lacor P, Larson J, Condie BG, Guidotti A, Costa E (2001) Down-regulation of dendritic spine and glutamic acid decarboxylase 67 expressions in the reelin haploinsufficient heterozygous reeler mouse. *Proc Natl Acad Sci U S A* 98:3477–3482.
- Matsuki T, Pramatarova A, Howell BW (2008) Reduction of Crk and CrkL expression blocks reelin-induced dendritogenesis. *J Cell Sci* 121:1869–1875.
- Matsunaga Y, Noda M, Murakawa H, Hayashi K, Nagasaka A, Inoue S, Miyata T, Miura T, Kubo KI, Nakajima K (2017) Reelin transiently promotes N-cadherin-dependent neuronal adhesion during mouse cortical development. *Proc Natl Acad Sci U S A* 114:2048–2053.
- Montgomery JC, Guarnieri MH, Tartaglia KE, Flaherty LA (1994) High-resolution genetic map and YAC contig around the mouse neurological locus reeler. *Mamm Genome* 5:756–761.
- Morrill SA, Amon A (2019) Why haploinsufficiency persists. *Proc Natl Acad Sci U S A* 116:11866–11871.
- Nakano Y, Kohno T, Hibi T, Kohno S, Baba A, Mikoshiba K, Nakajima K, Hattori M (2007) The extremely conserved C-terminal region of Reelin is not necessary for secretion but is required for efficient activation of downstream signaling. *J Biol Chem* 282:20544–20552.
- Niu S, Renfro A, Quattrocchi CC, Sheldon M, D’Arcangelo G (2004) Reelin promotes hippocampal dendrite development through the VLDLR/ApoER2-Dab1 pathway. *Neuron* 41:71–84.
- Noctor SC, Flint AC, Weissman TA, Dammerman RS, Kriegstein AR (2001) Neurons derived from radial glial cells establish radial units in neocortex. *Nature* 409:714–720.
- Nullmeier S, Panther P, Dobrowolny H, Frotscher M, Zhao S, Schwegler H, Wolf R (2011) Region-specific alteration of GABAergic markers in the brain of heterozygous reeler mice. *Eur J Neurosci* 33:689–698.
- Ogawa M, Miyata T, Nakajima K, Yagyu K, Seike M, Ikenaka K, Yamamoto H, Mikoshiba K (1995) The reeler gene-associated antigen on Cajal-Retzius neurons is a crucial molecule for laminar organization of cortical neurons. *Neuron* 14:899–912.

- Ohtaka-Maruyama C, Okado H (2015) Molecular pathways underlying projection neuron production and migration during cerebral cortical development. *Front Neurosci* 9:447.
- Olson EC, Kim S, Walsh CA (2006) Impaired neuronal positioning and dendritogenesis in the neocortex after cell-autonomous *Dab1* suppression. *J Neurosci* 26:1767–1775.
- Pramatarova A, Ochalski PG, Chen K, Gropman A, Myers S, Min KT, Howell BW (2003) Nck beta interacts with tyrosine-phosphorylated disabled 1 and redistributes in Reelin-stimulated neurons. *Mol Cell Biol* 23:7210–7221.
- Qiu S, Korwek KM, Pratt-Davis AR, Peters M, Bergman MY, Weeber EJ (2006) Cognitive disruption and altered hippocampus synaptic function in Reelin haploinsufficient mice. *Neurobiol Learn Mem* 85:228–242.
- Sakai K, Shoji H, Kohno T, Miyakawa T, Hattori M (2016) Mice that lack the C-terminal region of Reelin exhibit behavioral abnormalities related to neuropsychiatric disorders. *Sci Rep* 6:28636.
- Sánchez-Hidalgo AC, Martín-Cuevas C, Crespo-Facorro B, Garrido-Torres N (2022) Reelin alterations, behavioral phenotypes, and brain anomalies in schizophrenia: a systematic review of insights from rodent models. *Front Neuroanat* 16:844737.
- Sawahata M, Asano H, Nagai T, Ito N, Kohno T, Nabeshima T, Hattori M, Yamada K (2021) Microinjection of Reelin into the mPFC prevents MK-801-induced recognition memory impairment in mice. *Pharmacol Res* 173:105832.
- Schindelin J, Arganda-Carreras I, Frise E, Kaynig V, Longair M, Pietzsch T, Preibisch S, Rueden C, Saalfeld S, Schmid B, Tinevez JY, White DJ, Hartenstein V, Eliceiri K, Tomancak P, Cardona A (2012) Fiji: an open-source platform for biological-image analysis. *Nat Methods* 9:676–682.
- Schuman B, Dellal S, Prönnke A, Machold R, Rudy B (2021) Neocortical layer 1: an elegant solution to top-down and bottom-up integration. *Annu Rev Neurosci* 44:221–252.
- Sekine K, Honda T, Kawauchi T, Kubo K, Nakajima K (2011) The outermost region of the developing cortical plate is crucial for both the switch of the radial migration mode and the *Dab1*-dependent “inside-out” lamination in the neocortex. *J Neurosci* 31:9426–9439.
- Sekine K, Kawauchi T, Kubo K, Honda T, Herz J, Hattori M, Kinashi T, Nakajima K (2012) Reelin controls neuronal positioning by promoting cell-matrix adhesion via inside-out activation of integrin $\alpha 5 \beta 1$. *Neuron* 76:353–369.
- Sheldon M, Rice DS, D’Arcangelo G, Yoneshima H, Nakajima K, Mikoshiba K, Howell BW, Cooper JA, Goldowitz D, Curran T (1997) Scrambler and *yotari* disrupt the disabled gene and produce a reeler-like phenotype in mice. *Nature* 389:730–733.
- Sohal VS, Zhang F, Yizhar O, Deisseroth K (2009) Parvalbumin neurons and gamma rhythms enhance cortical circuit performance. *Nature* 459:698–702.
- Solari SV, Stoner R (2011) Cognitive consilience: primate non-primary neuroanatomical circuits underlying cognition. *Front Neuroanat* 5:65.
- Soltész I, Losonczy A (2018) CA1 pyramidal cell diversity enabling parallel information processing in the hippocampus. *Nat Neurosci* 21:484–493.
- Sweet HO, Bronson RT, Johnson KR, Cook SA, Davisson MT (1996) Scrambler, a new neurological mutation of the mouse with abnormalities of neuronal migration. *Mamm Genome* 7:798–802.
- Tabata H, Nakajima K (2001) Efficient in utero gene transfer system to the developing mouse brain using electroporation: visualization of neuronal migration in the developing cortex. *Neuroscience* 103:865–872.
- Tabata H, Nakajima K (2003) Multipolar migration: the third mode of radial neuronal migration in the developing cerebral cortex. *J Neurosci* 23:9996–10001.
- Tabata H, Nakajima K (2008) Labeling embryonic mouse central nervous system cells by in utero electroporation. *Dev Growth Differ* 50:507–511.
- Tabata H, Kanatani S, Nakajima K (2009) Differences of migratory behavior between direct progeny of apical progenitors and basal progenitors in the developing cerebral cortex. *Cereb Cortex* 19:2092–2105.
- Tremolizzo L, Carboni G, Ruzicka WB, Mitchell CP, Sugaya I, Tueting P, Sharma R, Grayson DR, Costa E, Guidotti A (2002) An epigenetic mouse model for molecular and behavioral neuropathologies related to schizophrenia vulnerability. *Proc Natl Acad Sci USA* 99:17095–17100.
- Trommsdorff M, Gotthardt M, Hiesberger T, Shelton J, Stockinger W, Nimpf J, Hammer RE, Richardson JA, Herz J (1999) Reeler/Disabled-like disruption of neuronal migration in knockout mice lacking the VLDL receptor and ApoE receptor 2. *Cell* 97:689–701.
- Veitia RA, Potier MC (2015) Gene dosage imbalances: action, reaction, and models. *Trends Biochem Sci* 40:309–317.
- Wang L, Zhao D, Wang M, Wang Y, Vreugdenhil M, Lin J, Lu C (2019) Modulation of hippocampal gamma oscillations by dopamine in heterozygous *eeeler* mice in vitro. *Front Cell Neurosci* 13:586.
- Wang X, Qiu R, Tsark W, Lu Q (2007) Rapid promoter analysis in developing mouse brain and genetic labeling of young neurons by doublecortin-DsRed-express. *J Neurosci Res* 85:3567–3573.
- Ware ML, Fox JW, González JL, Davis NM, Lambert de Rouvroit C, Russo CJ, Chua SC Jr, Goffinet AM, Walsh CA (1997) Aberrant splicing of a mouse disabled homolog, *mdab1*, in the scrambler mouse. *Neuron* 19:239–249.
- Yoneshima H, Nagata E, Matsumoto M, Yamada M, Nakajima K, Miyata T, Ogawa M, Mikoshiba K (1997) A novel neurological mutant mouse, *yotari*, which exhibits reeler-like phenotype but expresses CR-50 antigen/reelin. *Neurosci Res* 29:217–223.
- Yoo DY, Yoo KY, Choi JW, Kim W, Lee CH, Choi JH, Park JH, Won MH, Hwang IK (2011) Time course of postnatal distribution of doublecortin immunoreactive developing/maturing neurons in the somatosensory cortex and hippocampal CA1 region of C57BL/6 mice. *Cell Mol Neurobiol* 31:729–736.